OCS Study
BOEM 2018-053

Impact Assessment and Mitigation of Offshore Wind Turbines on High Frequency Coastal Oceanographic Radar

US Department of the Interior
Bureau of Ocean Energy Management
Office of Renewable Energy Programs

OCS Study
BOEM 2018-053

Impact Assessment and Mitigation of Offshore Wind Turbines on High Frequency Coastal Oceanographic Radar

August 2018

Authors:
Dale Trockel, Irene Rodriguez-Alegre, Donald Barrick, Chad Whelan

Prepared under M16PC00017
By
CODAR Ocean Sensors
1914 Plymouth Street,
Mountain View, CA 94043

US Department of the Interior
Bureau of Ocean Energy Management
Office of Renewable Energy Programs

BOEM
Bureau of Ocean Energy Management

DISCLAIMER

Study concept, oversight, and funding were provided by the US Department of the Interior, Bureau of Ocean Energy Management (BOEM), Environmental Studies Program, Washington, DC, under Contract Number M16PC00017. This report has been technically reviewed by BOEM, and it has been approved for publication. The views and conclusions contained in this document are those of the authors and should not be interpreted as representing the opinions or policies of the US Government, nor does mention of trade names or commercial products constitute endorsement or recommendation for use.

REPORT AVAILABILITY

To download a PDF file of this report, go to the US Department of the Interior, Bureau of Ocean Energy Management Data and Information Systems webpage (http://www.boem.gov/Environmental-Studies-EnvData/), click on the link for the Environmental Studies Program Information System (ESPIS), and search on 2018-053. The report is also available at the National Technical Reports Library at https://ntrl.ntis.gov/NTRL/.

CITATION

Trockel D, Rodriguez-Alegre I, Barrick D, Whelan C. 2018. Impact Assessment and Mitigation of Offshore Wind Turbines on High Frequency Coastal Oceanographic Radar. Sterling, VA: US Department of the Interior, Bureau of Ocean Energy Management. OCS Study BOEM 2018-053. 49 p.

ACKNOWLEDGMENTS

CODAR would like to acknowledge the following people and organizations for their efforts in making this program a success. First, we would like to thank Dr. John Vesecky, Professor Emeritus at University of California, Santa Cruz, for joining our progress meetings and for providing his assistance and insight into our efforts. Dr. Vesecky has also been a mentor and Ph.D. advisor to Ms. Irene Rodriguez-Alegre who has been a key component of our efforts. Second, we'd like to thank Dr. Hugh Roarty, Rutgers University & Mid-Atlantic Regional Association Coastal Ocean Observing System, and his team for maintaining high data quality from the HF Radar stations involved in this study. Third, we would like to thank the NOAA IOOS program office for funding the HFR network involved in this program and, in particular, Dr. Jack Harlan who recognized early on that this issue is an important one for the integrity of the national network. And, finally, we would like to thank Dr. Mary Boatman and her team at the BOEM Office of Renewable Energy Programs for providing the resources to do such an in-depth study and for their guidance throughout the program.

Contents

List of Figures

List of Tables

List of Abbreviations and Acronyms

BLCK	Block Island SeaSonde Radar Site
BOEM	Bureau of Ocean Energy Management
FFT	Fast Fourier Transform
FMCW	Frequency Modulated Continuous Waveform
FOL	First Order Lines
HFR	High Frequency Radar
NEC	Numerical Electromagnetic Code
RCS	Radar Cross Section
RPM	Rotations Per Minute

1 Introduction

The U.S. currently has a national network of more than 140 coastal High Frequency radars (HFR). The two-dimensional surface current data obtained from this network is invaluable for multiple applications. The U.S. Coast Guard assimilates the HFR data into models to boost reliability and narrow search areas for people and vessels lost at sea. Similarly, the sea surface current measurements help focus oil spill cleanup efforts. More recently, the National Weather Service has begun assessing HFR wave measurements for wave forecasting. Other applications of the national network include tsunami detection (outputs of which are transmitted to NOAA's Tsunami Warning Center), wind measurements and vessel detection among others.

Observations (Wyatt, Robinson and Howarth 2011) indicate that the spinning blades of offshore wind turbines cause interference in HF radars. In 2016, the first five offshore wind turbines in the USA were installed off Block Island, Rhode Island (RI). Additional wind farms, with many more turbines, are currently in the planning phase. It is therefore crucial that we understand the possible impact of these wind farms on the national radar network, and that we develop techniques to mitigate the impact of turbine interference on all the radar data products.

In September 2016, CODAR began an investigation (BOEM Contract M16PC00017) to study the impact of wind turbine interference on HF radar. Data was collected for a two-year period from six HF radar sites near the five turbines installed off the Southern coast of Block Island, RI. The focus of this work is to characterize the interference, quantify the impact, and investigate mitigation techniques. This study has laid the groundwork for future work by developing expertise and software tools for analyzing HFR data for turbine interference.

In the main body of this report, we present the key findings of the work completed under contract M16PC00017, as well as suggestions for the next steps. The key findings and next step are followed by seven appendices detailing the methods and findings of the work done.

Appendix A contains the NEC Technical Summary. The summary contains detail of the numerical simulation methods used to model and study wind turbine interference in costal HFR. In Appendix A we show the simulation results for frequencies commonly used for costal HFR including, 5 MHz, 13 MHz, 25 MHz, and 42 MHz.

In Appendix B, we describe the characteristics of the turbine interference in range-Doppler space. We derive a function relating the rotation rate of the turbine to the structure of the interference found in range-Doppler space of a SeaSonde cross-spectra. To Characterize wind turbine interference, we use the periodicity of the radar cross section (RCS) of a rotating wind turbine. The interference found in HF-radar resulting from a wind turbine is a consequence of the amplitude modulation of the signal reflected from the turbine, rather than a Doppler shift due to the velocity. As the turbine blades rotate, the RCS of the turbine changes, causing a proportional change in the voltage signal at the receiver.

The results of our impact assessment obtained from field data are presented in Appendix C. The impact assessment identifies several ways in which wind turbine interference impact the integrity of the HFR current measurements. The different mechanisms identified in Appendix C, are crucial to the development of mitigation techniques presented in Appendix D.

Appendix D contains the details on the mitigation methods we developed and tested. We present four different mitigation methods and test their effectiveness at reducing the impacts of wind turbine interference. We find that using estimates of the rotation rate of the wind turbines, allows us to effectively reduce the impacts of wind turbine interference for small wind farms.

The final three appendices, Appendix E, Appendix F, and Appendix G, contained more details on some of the work presented in the first four appendices. Appendix E reviews the frequency modulated complex waveform (FMCW) processing algorithm used by SeaSondes to obtain current measurements from the voltage signal from the receiver. Appendix F contains a description of the video analysis methods that were used to extract wind turbine rotation rates from videos. The methods used to estimate the wind turbine rotation rate from our SeaSonde cross-spectra are detailed in Appendix F.

2 Key Findings

The Key Findings of the study are:

- Wind turbine interference is caused by the amplitude modulation of the turbine's radar cross-section.
- The location of the wind turbine interference in the Doppler spectrum is predictable and can be determined from the rotation rate of the wind turbine.
- Wind turbine interference can be simulated in SeaSonde data using Numerical Electromagnetic Code (NEC) tools for both assessing the impact of wind turbine interference as well as designing mitigation methods.
- Wind turbine interference impacts the SeaSonde ocean current measurements in three ways:
    - Biasing the measurement of the true background noise level (affecting the sea echo identification algorithms)
    - Changing the boundaries of the requisite sea echo peaks by mischaracterizing turbine echoes as part of the sea echo
    - Changing the bearing assignment for the radial current vectors by causing turbine echoes to be convolved within the sea echo.
- Mitigation techniques that remove wind turbine interference from the sea echo peaks alone are insufficient and still lead to errors in the current measurements. The wind turbine interference outside the sea echo must be filtered as well.
- Using known bearings and a filter will at best remove a small portion of the wind turbine interference.
- Mitigation methods that remove signals from the Doppler spectrum based on the wind turbine rotation rate estimates are effective methods of mitigating wind turbine interference. Wind turbine rotation rates can be estimated from SeaSonde cross-spectra; it would be more successful if turbine RPMs were provided by the turbine operator.

3 Next Steps

Building upon the underpinning of the previous study, there are key areas that need continued effort to bring the mitigation techniques to operational status:

1. Extending the existing simulations to include interference from wind farms with an arbitrary number of inhomogeneously configured and rotating wind turbines.

2. Assessing the impact of turbine interference on secondary data products (e.g., wave heights and tsunami warnings required by the National Weather Service).
3. Development of a real-time mitigation solution.
4. Continuing monitoring and testing of mitigation techniques at Block Island as a primary test bed.

It is vital to develop mitigation software for the U.S. national HFR network before much larger offshore wind farms are constructed. Furthermore, it is necessary to continue to collect data to test mitigation methods and measure the impact on the secondary data products mentioned above. In the absence of data obtained from individual radar sites affected by wind turbine interference or in cases of previously unseen wind farm scales, simulations can provide a means to test mitigation techniques for existing HFR stations. Additionally, simulations allow us to vary parameters in our data such as the turbine positions, turbine rotation rates, blade-plane angle, number of turbines, and signal to noise ratio of the resulting interference. In the work contained in this report, we used the numerical electromagnetic code (NEC) to simulate the radar cross-section of the wind turbines from which we were able to approximate and verify a turbine's interference. Expansion of the numerical data simulation tools developed in this study would allow for an arbitrary number of turbines. Furthermore, it would allow each turbine to have different characteristics, (i.e., blade length, mast height, RPM, etc.).

Once simulation models have been developed and the resulting data have been verified, investigation of the scalability of the mitigation techniques developed in this study could be completed. Additionally, simulated data can be used to assess the impact of wind turbine interference on secondary data test products such as drifter simulations, search and rescue, tsunami warning, and waves. Simulations make it easy to vary parameters such as the noise floor, and the signal-to-noise ratio of the turbine interference, which allow testing of the impact in a range of possible background conditions.

As the number of offshore wind farms increases, real-time mitigation software will become increasingly necessary to preserve the integrity of the national network of coastal HF radars. During this study, we developed a radial current-flagging method to inform radar operators which radial vectors could be affected by turbine interference. However, no real time solution was developed. The next step is to implement the method into real-time software that can be deployed at any site. The next steps towards developing a real time mitigation solution include:

1. Integrate the cross spectra Doppler-bin flagging with the radial current processing software used on SeaSonde.
2. Integrate the radial vector filtering with the SeaSonde radial averaging software.
3. Update the mitigation routines currently written in Python into a compiled language suitable for real-time field use.
4. Integrate the real-time algorithms into existing SeaSonde coastal radars and ensure total compatibility with the many other data processing functions underway that provide environmental information needed by the government and other agencies.

While simulations are incredibly valuable, the radar sites at Block Island will continue to provide us the opportunity to test new mitigation techniques as well as validate our simulation models. Additionally, this study contains no radar data from a 13 MHz system that has been impacted by turbine interference. To fill this gap, it would be important to analyze data from a 13 MHz system with turbine interference.

4 Bibliography

Barrick, Donald. 1973. *FM/CW Radar Signals and Digital Processing.* NOAA Technical Report, U.S, U.S. Department of commerce, Boulder: NOAA.

Bradski, G. 2000. "OpenCV." *Dr. Dobb's Journal of Software Tools.*

Burke, Gerald J., A. J. Poggio, J. C. Logan, and J. W. Rockway. 1979. "Numerical electromagnetic code (NEC)." *International Symposium on Electromagnetic Compatibility, 1979.* IEEE. 1-3.

Challa, Subhash, Mark R Morelande, Darko Mušicki, and Robin J. Evans. 2011. *Fundamentals of Object Tracking.* New York: Cambridge University Press.

KaewTraKulPong, P., and R. Bowden. 2002. "An improved adaptive background mixture model for real-time tracking with shadow detection." In *Video-based surveillance systems*, by Graeme A. Jones Nikos Paragios Carlo S. Regazzoni. New York, New York: Springer.

Killick, Rebecca, and Idris A. Eckley. 2014. "Changepoint: An R Package for Changepoint Analysis." *Journal of Statistical Software* 58 (3): 1-19.

Killick, Rebecca, Kaylea Haynes, and Idris A. Eckley. 2016. "Changepoint: An R package for changepoint analysis."

Killick, Rebecca, P. Fearnhead, and Idris A. Eckley. 2011. "Optimal detection of changepoints with a linear computational cost." *ArXiv e-prints.*

Lipa, B. J., Bruce Nyden, D. S. Ullman, and E. Terrill. 2006. "SeaSonde radial velocities: derivation and internal consistency ." *IEEE J. Ocean. Eng* 31 (4): 850-861.

Teague, Calvin c., and Donald E. Barrick. 2012. "Estimation of wind turbine radar signature at 13.5 MHz." *Oceans.* IEEE. 1-4.

Wyatt, L. R., A. M. Robinson, and M. J. Howarth. 2011. "Wind farm impacts on HF radar current and wave measurements in Liverpool Bay." *OCEANS.* IEEE-Spain. 1-3.

Appendix A: NEC Technical Summary

There are over 100 coastal ocean observing high frequency (HF) radar systems in the U.S. With five offshore wind turbines already installed and plans to install several more in the coming years, it is important to understand how these turbines may affect the operation of the National Integrated Ocean Observing System (IOOS) coastal observing HF radar network. The purpose of this Appendix is to show the expected wind turbine impact on SeaSonde spectra using simulated data. In particular, we look at the characteristics of the spectral interference introduced by the turbines and how it varies with the orientation of the turbine to the radar receiver and the transmitted frequency.

Though a turbine is a stationary hard target, the amplitude of the returned signal varies as the blades rotate. This amplitude modulation is periodic and repeats itself every 120° due to the symmetry of a three bladed wind turbine. Furthermore, the amplitude of the return signal from the turbine blades can be deduced from the target's radar cross-section (RCS). We approximate the RCS using the Numerical Electromagnetic Code (NEC), (Burke, et al. 1979). We extend the work in Teague and Barrick (Teague and Barrick 2012) using a wider range of frequencies, including 5 MHz, 13.5MHz, 25 MHz, and 42 MHz commonly employed by SeaSonde, and use the resulting RCS to calculate a voltage signal. This signal is run through CODAR's frequency-modulated continuous wave (FMCW) processing, and Range Doppler Spectra are obtained. The qualitative differences in spectra due to the nacelle angle and transmitted frequency are explored.

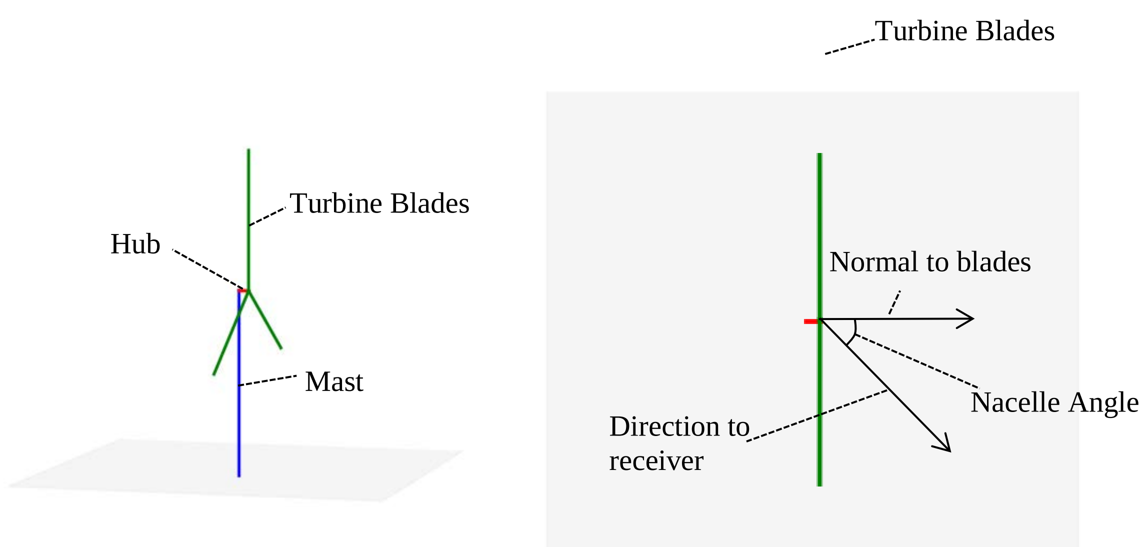

Figure 1. NEC Wire Frame Model
Side view (left) and top view (right) of wire frame model used for NEC simulations. The blades are shown in green, the hub in red, and the mast is shown in blue.

A.1 NEC

To use NEC, targets are approximated with wire models, yielding best results with approximately ten wire segments per half a wavelength of the transmitted signal. For the turbine wire models, we use lengths of the blades, mast, and generator hub—approximately the same as on the turbines installed by Deepwater Wind at Block Island. In **Figure 1**, the five-wire model used for simulations is shown. Three wires are used for each of the three blades (shown in green), one for the mast (shown in blue), and one for the generator hub body (shown in red). These are joined electrically to each other at their intersection.

While separate wires are used for each part of the turbine model, they are all connected, and the mast is connected to the ground plane (representing the sea surface). The orientation of the turbine to the receiver is defined by the angle of the vector normal to the blade plane makes with a vector in the direction of the receiver. Hereafter, we will refer to this angle as the nacelle angle. A wire diameter of 0.2 m is used for each wire, with no tapering from end to end; these factors are relatively unimportant in the overall target RCS. A complete set of parameters used for the wireframe model can be found in Table 1.

When a plane wave excitation card is used as an input to NEC, the resulting radiation pattern in the output from NEC is given in terms of the normalized RCS. A Python script was used to create single NEC input file for each frequency. The input files contain the NEC card-deck simulating lines needed to obtain a radiation pattern for varying BPAs and rotation angles.

A series of BPAs ranging from 0° to 90° in 5° increments were used. Also, for each nacelle angle NEC input cards are made for a series of rotation angles, starting at 0° of rotation and ending at 120° in 0.5° increments, with 0° corresponding to when a reference blade is in the upward vertical position. Once the input file has been created NEC is used to calculate the corresponding RCS for each nacelle angle and rotation angle.

A.1.1 RCS

For each nacelle angle and rotation angle, there is a corresponding radiation pattern in the NEC output file giving a gain, which is the RCS in dB relative to the wavelength, and an RCS signal phase. A Python script is then used to parse the output file from NEC extracting the phase and gain for each nacelle angle, θ, and rotation angle, ϕ. The gain, $g(\phi,\theta)$, and phase, $\alpha(\phi,\theta)$ can then be used to reconstruct the corresponding complex voltage signal as

$$v^{NEC}(\phi,\theta)=10^{\frac{g(\phi,\theta)}{20}}\exp(i\alpha(\phi,\theta)). \tag{0.1}$$

The RCS is then given by

$$\sqrt{RCS}=\lambda 20\log_{10}(g(\phi,\theta)). \tag{0.2}$$

where λ is the radar wavelength.

Table 1. Parameters used with NEC

Parameter	Value
Mast Height	100 m
Hub Length	10 m
Blade Length	40 m
Number of Blade Segments	20
Number of Mast Segments	50
Number of Hub Segments	2
Frequencies	5 MHz, 13.5 MHz, 25 MHz, 42 MHz
Sweep Band width	25 KHz

In Figure 2, we plot the square root of the RCS over a 120° rotation period for four BPAs (0°, 30°, 60°, 90°) for a 5 MHz (top left), 13.5 MHz (top right), 25 MHz (bottom left), and 42 MHz (bottom right) plane wave. For all frequencies, there are more oscillations in the RCS, over one l20° rotation interval, as the nacelle angle increases. Furthermore, as the frequency increases so does the amount of high-frequency oscillations, as expected when the wavelength becomes small with respect to target dimensions.

One last thing to note in Figure 2, is that for all frequencies and all BPAs, the RCS changes most rapidly once the blades have rotated around 60°. Since we start with a reference blade in the vertical position, at 60° one of the other blades is in the bottom-most vertical position in line with the mast. Thus, the abrupt changes in the RCS are due to the integration (strong coupling) of the mast with one of the blades.

A.1.2 RCS Fast Fourier Transform (FFT)

As the rotation angle varies in time, equation (0.1) gives a time series of the voltage response. Python was used to calculate the FFT of equation (0.1) over one 120° rotation interval. Due to the three-fold symmetry of the blades, it was not necessary to use a window of any kind to suppress side-lobes.

We plot the results for each of the test frequencies for BPAs of 0° and 60°, respectively, in Figure 3 and Figure 4. In each of the plots, we remove the fundamental mode zero to aid in comparisons.

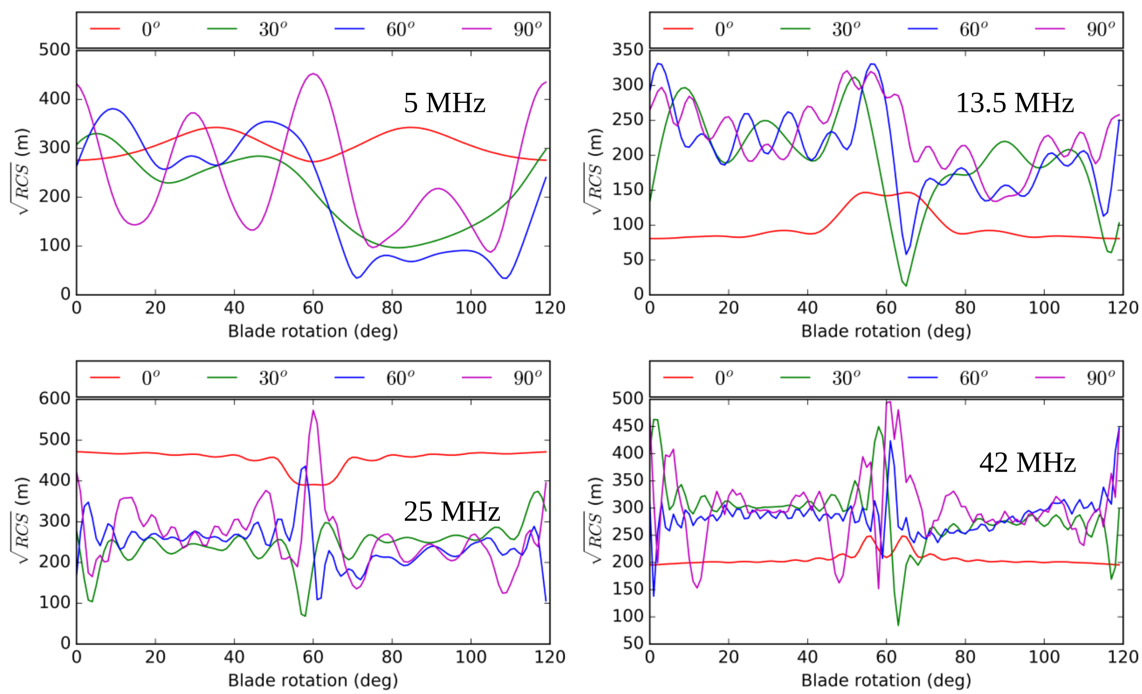

Figure 2. Radar cross-section

The RCS of a wind turbine as the blades rotate 120° for 5 MHz (top left), 13.5 MHz (top right), 25 MHz (bottom left), and 42 MHz (bottom right). For each frequency, the RCS is plotted for nacelle angles of 0° (red), 30° (green), 60° (blue), and 90° (magenta).

There are three important observations of note. First, the energy in the harmonic modes is symmetric about the zero mode, only when the nacelle angle is 0°. Teague and Barrick (Teague and Barrick 2012) showed that this is caused by the interactions of the mast and the blades, and that symmetry can be regained by running the model with the blades floating in free space with no mast or hub. Second, by increasing the nacelle angle, there is an increase in energy in the higher modes, while simultaneously decreasing the amount of energy found in any single mode. Lastly, increasing the frequency also spreads the energy to higher modes while decreasing the maximum energy in any mode. We also should remark that we have only plotted the first 20 positive and negative fundamental modes; however, in the case of the higher frequencies (*i.e.*, 25 MHz and 42 MHz) there can be as many as 50 positive and negative modes with significant energy.

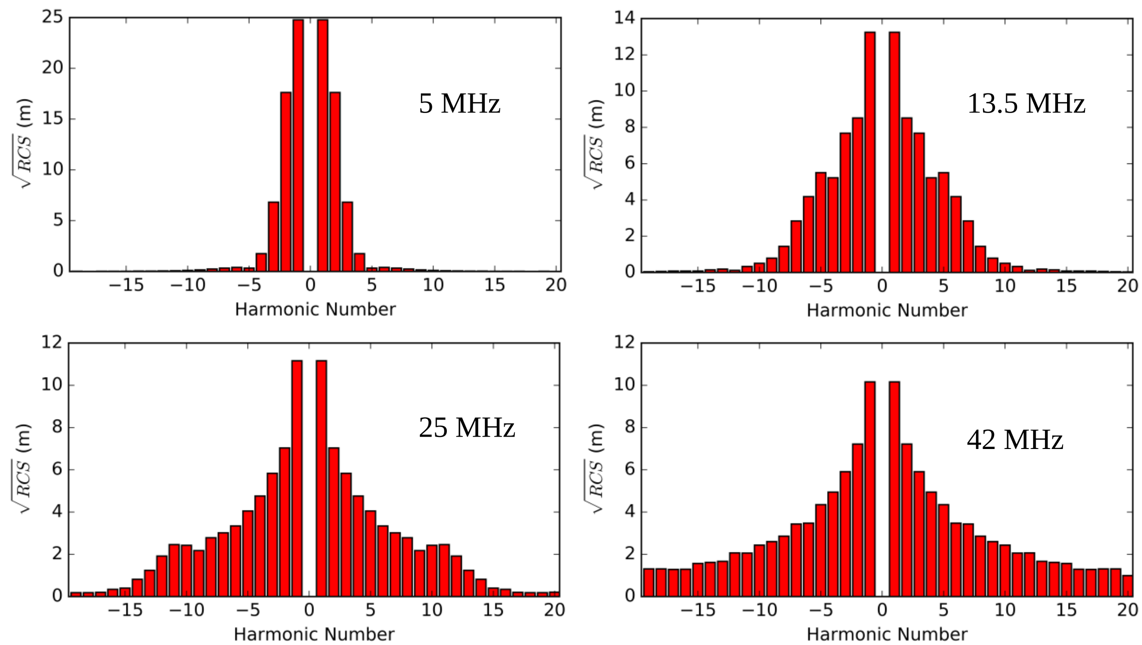

Figure 3. Spectra of the RCS, nacelle angle of 0°
Plots only show energy in the first 20 positive and negative modes. Fundamental mode zero has been removed to aid in visualization. There is more spread in the spectral energy as frequency increases**.**

A.2 SeaSonde Spectra Simulation

The ultimate goal of the NEC simulations is to gain insight into the impact of turbines on SeaSonde cross spectra, from which currents are obtained. To do this, the voltage signal from the turbine obtained given in equation (0.1) must be multiplied by a complex multiplying factor to account for the time delay, given its range from the radar, and then processed with CODAR’s complex FMCW waveform and it’s demodulation/processing. We present the details of this process below. For an in-depth explanation of CODAR’s complex FMCW waveform and its demodulation/processing see (Barrick 1973).

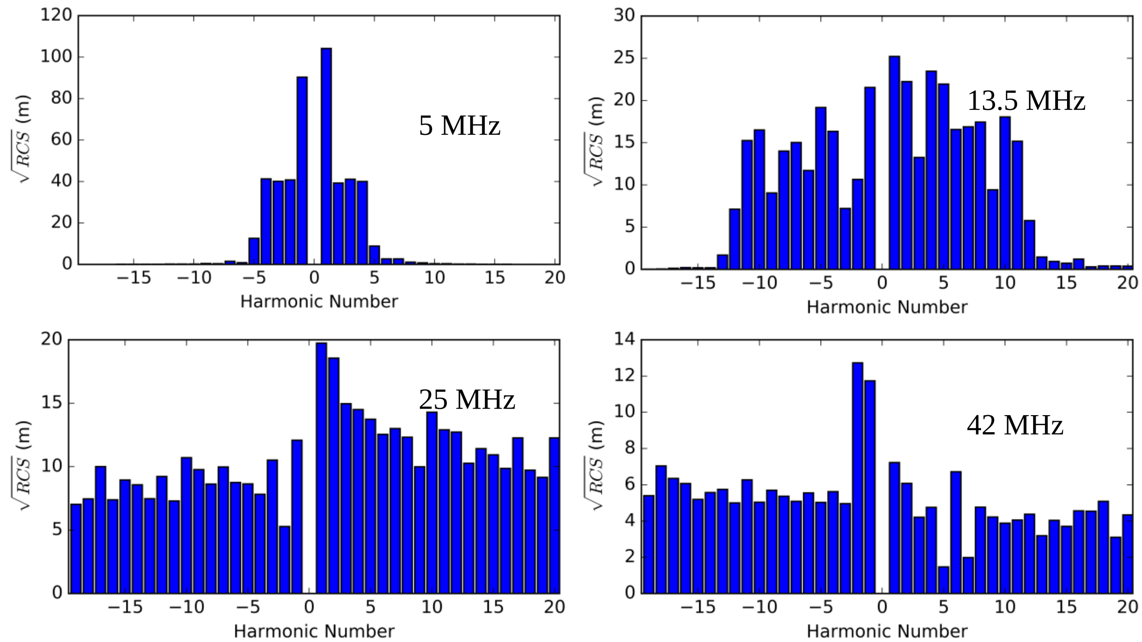

Figure 4. Spectra of the RCS, nacelle angle of 60°

Plots only show energy in the first 20 positive and negative modes. Fundamental mode zero has been removed to aid in visualization. There is more spread in the spectral energy as the frequency increases.

A.2.1 Complex Multiplying factor

Given a nacelle angle, θ, and a time series ϕ_n of *N* rotation angles we can use (0.1) to obtain a time series of corresponding voltages, v_n^{NEC}. To demodulate the signal and obtain the range and velocity of a target, we use CODAR's double FFT process, in which the range is recovered in the first FFT and the Doppler in the second. Thus, to accurately represent a turbine, the time series v_n^{NEC} must be adjusted by a complex multiplying factor—after demodulation in the receiver—that accounts for its time delay. This is given by

$$\exp(-i\vartheta_n), \tag{0.3}$$

with

$$\vartheta_n = 2\pi n \frac{2rB_{Sw}\Delta t}{cT_{Sw}}, \tag{0.4}$$

where *n* is the index of the specific analog to digital (A/D) output number (or harmonic of the fundamental at *n* = 1); r is the distance to the turbine in kilometers (*e.g.*, ~5 km for Block Island turbines); B_{Sw} is the sweep width in kHz (*e.g.*, 25 kHz for the long-range SeaSonde on Block Island); Δt is the A/D sample output interval in seconds, *i.e.*,

$\Delta t = \dfrac{1}{4096} = 244\,\mu s$ for the SeaSonde; c is the speed of light in kilometers per second (3e05 km/s); T_{Sw} is the sweep repetition period in seconds (1 second for Long-Range SeaSonde). Thus, combining (0.1) and (0.3) the resulting signal is given by:

$$v_n = \lambda 20\log_{10}(g_n)\exp(i\alpha_n)\exp(-i\vartheta_n) \qquad (0.5)$$

where $g_n = g(\phi_n, \theta)$ and $\alpha_n = \alpha(\phi, \theta)$.

A.2.2 Range and Doppler spectra

The sampling frequency is made the same as the A/D rate in CODAR receivers, which is 4096 Hz. Hence, for the first range FFT with the rotating turbine, we must sample its echo (via NEC) every 1/4096 second. Furthermore, the first FFT (to obtain range) is done every second (1 Hz) for the 5 MHz Block-Island long-range radar on the 4096 samples gathered. If one were to sample the RCS output of NEC over this period, NEC would need to be run 4096 times for any arbitrary selected rotation rate.

However, in order to study the signal of the turbine echo in the range of the Doppler spectra, namely how the Doppler spikes from the turbines beyond ±0.5 Hz will be falsely spread into other range cells, one must continue to gather subsequent 1-second time-series segments from the turbine echoes, over a period (for the 5 MHz systems) of 1024 seconds. So, a continuous time series of successive blade positions (and NEC RCS values) must continue until 4096 × 1024 = 4,194,304 (= 2^{24}) samples are collected. This is prohibitive in both computational time to run NEC as well as file management. To decrease the number of NEC RCS samples needed, we tested two methods: **decimation and interpolation**, which we outline below.

A.2.3 Decimation

The first method, decimation, significantly decreases the number of NEC RCS calculations needed while using exact values of the RCS for all echo samples. However, it is not easily extended to handle arbitrary rotation rates. We demonstrate the method for the case in which the turbine is spinning at 12 rotations per minute (RPM), 5 km from a 5 MHz radar with a sweep bandwidth of 25 kHz. This is similar to the conditions found on the Block Island system. If we calculated an NEC output for every one of the 4096 A/D outputs, the angle increment for this would have been 0.0176° per A/D sample output. This can be reduced to 128 angles with NEC outputs (rather than 4096), and process a 128-point FFT instead of 4096-point FFT. During the 1-second sweep interval, the blades rotate 72° at 12 RPM (or 0.2 rotations per second [RPS]). Dividing into 128 equal increments gives an angle increment of 0.5625°. So, rather than do the first FFT over 4096 points, we decimate the input to just 128 complex values spanning the 72° sector, each 0.5625°. Thus after the first range FFT, we are left with 64 positive range cells and 64 negative range cells. The negative range cells are always discarded leaving us with the 64 positive range cells which are the same as the first 64 positive range cells of the full 4096 FFT. In this way, we effectively decrease the number of NEC calculations from 4096 to 128 per sweep.

For the second Doppler FFT, we take advantage of the rotation rate and symmetry of the blades to reduce the total number of NEC calculations needed. One period, *i.e.*, the time it takes to spin 120°, is 120/72 =

1.6667 seconds. However, in one rotation (360°), the number of periods is an integer (360°/72° = 5). Hence, we could take five periods (one rotation), over 640 angle increments. Meaning, for the angle increments we have chosen (0.5625°), we only need to do 640 NEC calculations.

Then the next 80 points of the time series are repeats of the first 80. On and on, until the number exceeds 1024, when we are ready for our second (Doppler) FFT calculation.

Therefore, we can collect 1024 rows (over 1024 seconds) of these 64-point NEC complex outputs, with 64 points in each row. Then we take the 2nd Doppler transform over each of the 64 columns, the column length being 1024. This should give Doppler spectra for each of the 64 range cells, with the same time resolution as our present 5 MHz (long-range) radars. Each bin of the Doppler spectrum should be 1/1024 = 0.9766 milli-Hertz in width. Furthermore, for both the range and the Doppler FFT, we use a Hamming window to more closely approximate the SeaSonde signal processing.

For each of the test frequencies, we show the resulting range Doppler spectra using decimation for a nacelle angle of 0° and 60° in Figure 5 and Figure 6, respectively. Note how increasing the nacelle angle or the frequency increases the signal in the higher range cells.

A.2.4 Interpolation

The second way to decrease the number of outputs needed from NEC is to use interpolation. This has the advantage of being easy to extend to any rotation rate. However, it is not an exact solution and is only an approximation. Due to the smoothness of the RCS, as seen in Figure 2, the error should be small if sufficient samples are taken. We sampled the 120° interval every 0.25°. Thus, in more detail, given a series of gains and phases corresponding to a sequence of rotation angles, we approximate the value in between using linear interpolation.

We show the range Doppler plots created using linear interpolation in Figure 7 and Figure 8. Qualitatively the plots are similar, with the high amplitude spikes in the same range Doppler bins. Again, we see that increasing the nacelle angle or the frequency increases the signal in the higher range cells.

A.3 Concluding remarks

Simulations with NEC show an increase in both the number of range and Doppler cells impacted by a turbine echo as the nacelle angle increases or the frequency increases. However, while the number of cells increases, the maximum impact in any one cell is reduced. While we have only explored one rotation rate here, it should be noted that the location of the peaks in the range Doppler spectra due to the turbine echo shift position with a change in rotation rate. This means that on any radar there are rotation rates that will shift these peaks into the Bragg regions (*i.e.*, the regions of the spectra containing the sea echo) corrupting ocean surface current data.

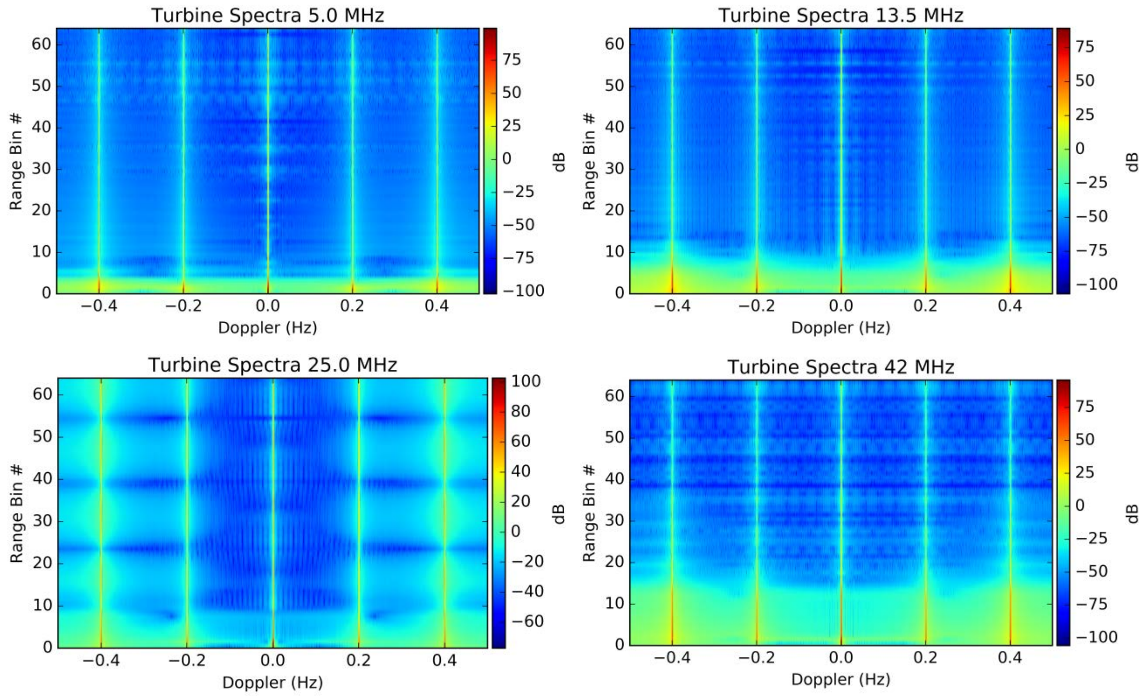

Figure 5. Range Doppler spectra using decimation and a nacelle angle of 0°
Range Doppler Plots from range corrected NEC outputs. A Hamming window has been used for both the range and Doppler FFT. Only the positive range bins are shown.

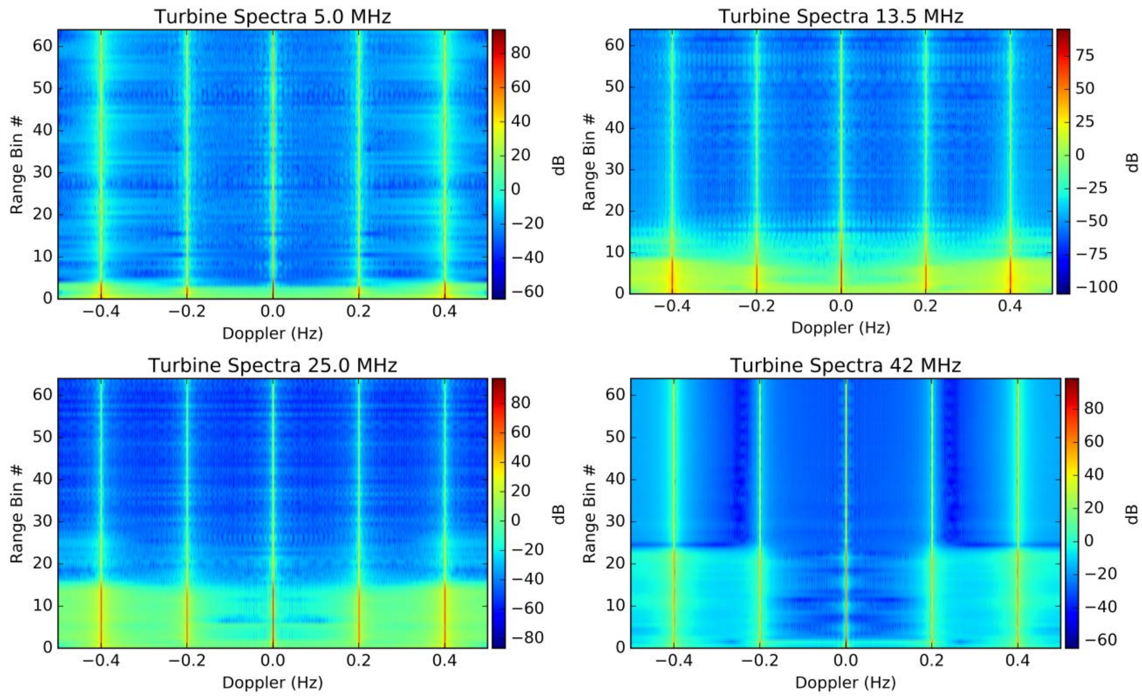

Figure 6. Range-Doppler spectra using decimation and a nacelle angle of 60°

Range Doppler Plots from range corrected NEC outputs. A Hamming window has been used for both the range and Doppler FFT. Only the positive range bins are shown.

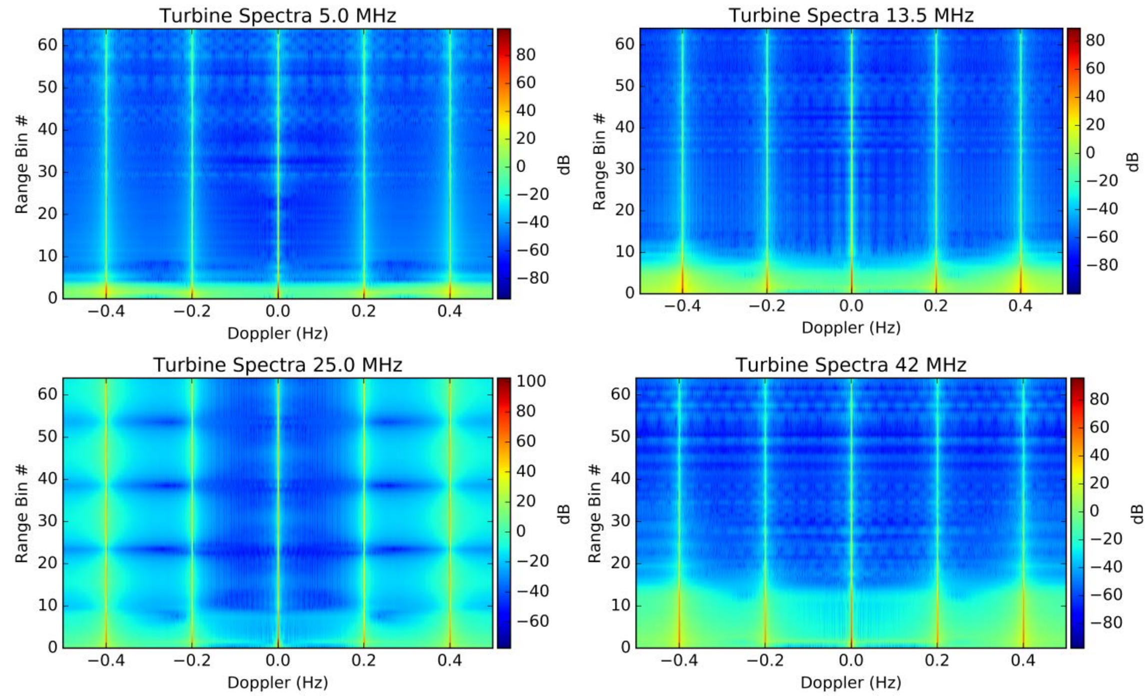

Figure 7. Range-Doppler spectra using interpolation and a nacelle angle of 0°

Range Doppler Plots from range corrected NEC outputs. A Hamming window has been used for both the range and Doppler FFT. Only the positive range bins are shown.

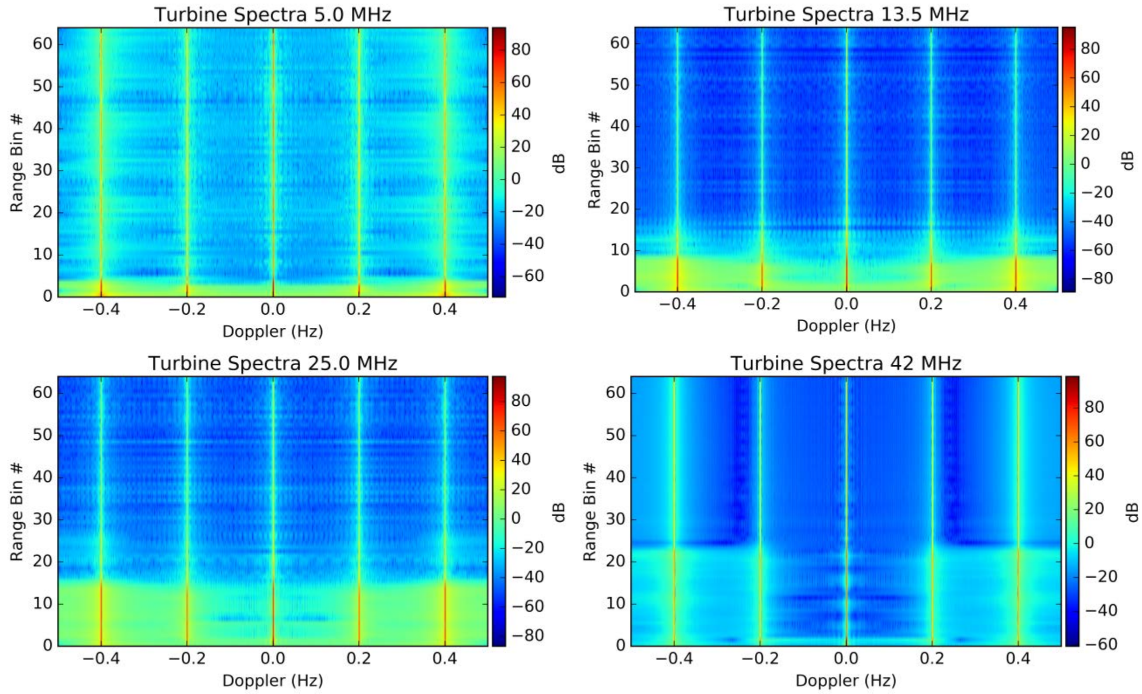

Figure 8. Range-Doppler spectra using interpolation and a nacelle angle of 60°
Range Doppler Plots from range corrected NEC outputs. A Hamming window has been used for both the range and Doppler FFT. Only the positive range bins are shown.

Appendix B: Analysis and Characterization of Wind Turbine Interference in HF Radar

The characterization of wind turbine interference in range-Doppler space of high-frequency radar data is an essential first step towards both assessing the impact of the interference as well as designing mitigation techniques. When wind turbines are in the radar measurement field, they introduce interference in multiple range-Doppler bins (Wyatt, Robinson and Howarth 2011). Depending on the location of the interference in range-Doppler space, it can be difficult to distinguish from sea echo and other types of interference. Teague and Barrick (Teague and Barrick 2012) used Numerical Electromagnetic Code (NEC) (Burke, et al. 1979) to model the radar cross-section (RCS) of a wind turbine as it rotates. Afterwards, they used Fourier analysis to demonstrate the amplitude modulation of the RCS as the blades rotate. They also observed that the angle between the normal vector of the plane containing the three turbine blades and the vector pointing to the radar receiver, hereafter referred to as the nacelle angle, changed the amount of energy in each of the harmonics components of the RCS function.

In this Appendix, we will extend the results of (Teague and Barrick 2012) by using NEC to simulate the RCS of the turbine rotating at different rates and BPAs. Once we obtain the RCS, we use it to estimate the complex voltage signal resulting from a wind turbine, expected at the receiver. The simulated complex voltage signal is processed using the double FFT method outlined in (Barrick 1973). This allows us to study the impact of wind turbine interference in the range-Doppler plane of SeaSonde cross-spectra. We then derive a closed-form solution for the range-Doppler bins in which we expect to find interference. Following the derivation, the predictive model is extended to incorporate the effects of under sampling. That is, we derive a functional expression giving the range and Doppler cells with interference that takes into account aliasing. The derived expression depends only on the rotation rate of the turbine blades. Following the derivation, we show that while the nacelle angle does not change the location of the range-Doppler cells that contain turbine interference, it does change their relative amplitudes. We finish the Appendix with a look at the impact of frequency and multiple turbines. We focus our analysis mainly on 4.538 MHz systems, the frequency of the long-range SeaSonde at Block Island. However, the closed form solutions and the techniques found herein apply to HF-radar systems of any frequency.

NOTE: Appendix B content is proprietary and will be provided with permission on request.

Appendix C: Wind Turbine Interference Impact Assessment

In Appendix B, we used Fourier analysis to derive closed-form solutions showing how and where wind turbine interference manifests itself in SeaSonde cross-spectra. We showed that the location of the interference depends on the frequency, sweep rate, and rotation rate of the wind turbines. However, the amplitude of the turbine interference depends on both the nacelle angle and the physical properties of the wind turbine. The results were confirmed by inspection of SeaSonde cross-spectra during times when the rotation rate of the wind turbine was known. However, the question of the impact of the interference on the sea current measurements remained. In this Appendix, we use numerical simulations along with observations of radar measurements to assess the impact of wind turbine interference. This study identifies three different mechanisms that impact the quality of the ocean current measurements: the measurement of the noise floor, changing the boundaries of the Bragg regions, or changing the bearing assignment to the radial current vectors.

The outline of this Appendix is as follows: We start with a description of the simulation method we use to test the impact of the wind turbine interference. We follow the simulation description with an overview of the video analysis techniques used to obtain rotation rates of the wind turbines in the Block Island wind farm. After the analysis techniques have been described, we investigate the impact of the turbine interference, looking directly at how the rotation rate influences the determination of the Bragg regions and how the current measurements are impacted. We then assess the impact of wind turbine interference on the 5 MHz radar at Block Island, by examining the frequency of each rotation rate. We then conclude with a discussion on the influence of the radar frequency and distance from the turbines.

C.1 Methods

It is difficult to measure the impact or wind turbine interference directly from radar data, as it is not possible to simultaneously collect HF radar data with and without wind turbine interference. Furthermore, there are often other types of interference (e.g., vessel echo and ionospheric interference) that further obfuscate the impact of the wind turbine interference. Beyond the challenges above, it would be difficult to collect sufficient data to show the dependence of any impacts on rotation rates and nacelle angles. To circumvent these challenges we utilize numerical simulations, which enables us to adjust and isolate the impact of the rotation rate and nacelle angle.

It is necessary to validate and calibrate any numerical model. We validate the simulations where possible using rotation rates and nacelle angles along with Doppler cross-spectra data collected from the BLCK (Block Island) SeaSonde. As there was no convenient source of rotation rates and nacelle angles, we rely on video cameras along with image processing scripts to extract the RPM and nacelle angle of each turbine. In the rest of this section, we describe the methods used to create the simulated cross-spectra. We follow the simulation description with an explanation of the video analysis techniques used to obtain rotation rates.

C.2 Simulations

To isolate the impact of wind turbine interference, we rely on a mix of simulations and measured data. We use NEC (Numerical Electromagnetic Code®) to simulate the wind turbine interference, which we add to SeaSonde cross-spectra collected in the absence of wind turbine interference.

The simulated data allow us to investigate the impact of operational parameters such as the rotation rates of the turbines and the angle of the nacelle. We focus our simulations on the cross-spectra as the current measurements are obtained directly from the cross-spectra. Furthermore, as we show below, the errors in the current measurements are introduced when extracting the current data from the cross-spectra.

Table 2. Dates and times sample cross-spectra were collected at BLCK

Year	Month	Day	Time
2016	March	22	00:00
2016	March	31	22:00
2016	April	4	00:00
2016	April	15	10:00
2016	May	5	01:00
2016	May	16	12:00
2016	June	1	05:00
2016	June	18	22:00
2016	July	7	04:00
2016	July	18	04:30
2016	August	1	17:00
2016	August	12	09:00

We used NEC as outlined in Appendix A to create the simulated wind turbine interference signals for a single turbine at input RPM and nacelle angle. See Figure 15 for two examples of wind turbine interference simulated with NEC. The simulated wind turbine interference is then scaled and added to a sample cross-spectra collected before the turbines were spinning. To increase statistical significance, we use a sample of twelve SeaSonde cross-spectra collected at the Block Island BLCK 4.538 MHz radar during spring and summer of 2016 before the wind farm was operational. The dates and times of sample cross-spectra are found in Table 3.

For each of the twelve dates found in Table 3, we generated a set of 1463 cross spectra with wind turbine interference, each corresponding to a specific RPM and nacelle angle pair. In the set of 1463 simulated cross-spectra, the rotation rates range from 4 to 11.6 rpm at 0.1 increments, while the nacelle angle interval ranges from 0° to 90° at 1° increments.

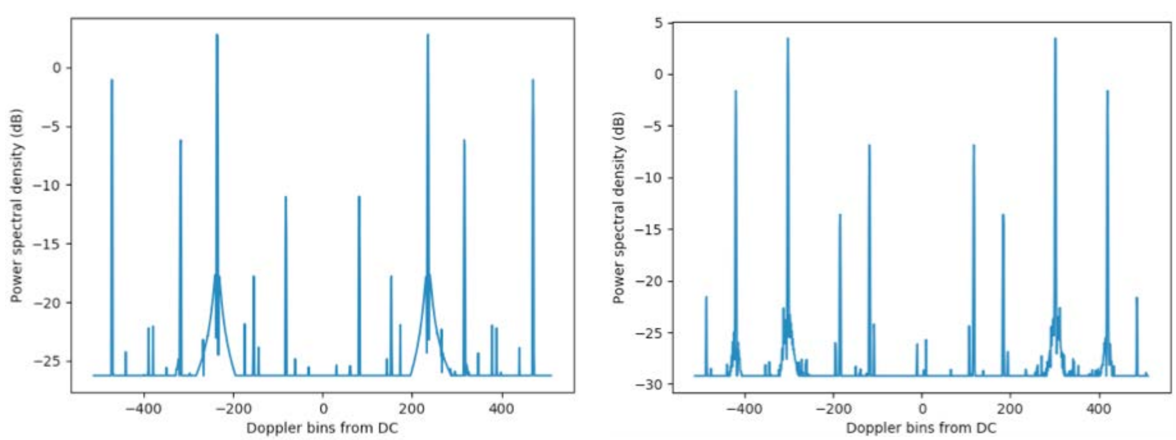

Figure 9. Simulated wind turbine interference.
Left: wind turbine interference in the 1024 Doppler bins of the first range cell simulated with NEC with the nacelle angle at 0° and the rotation rate at 4.6 RPM. Right: wind turbine interference in the 1024 Doppler bins of the first range cell simulated with NEC with the nacelle angle at 0° and the rotation rate at 5.9 RPM.

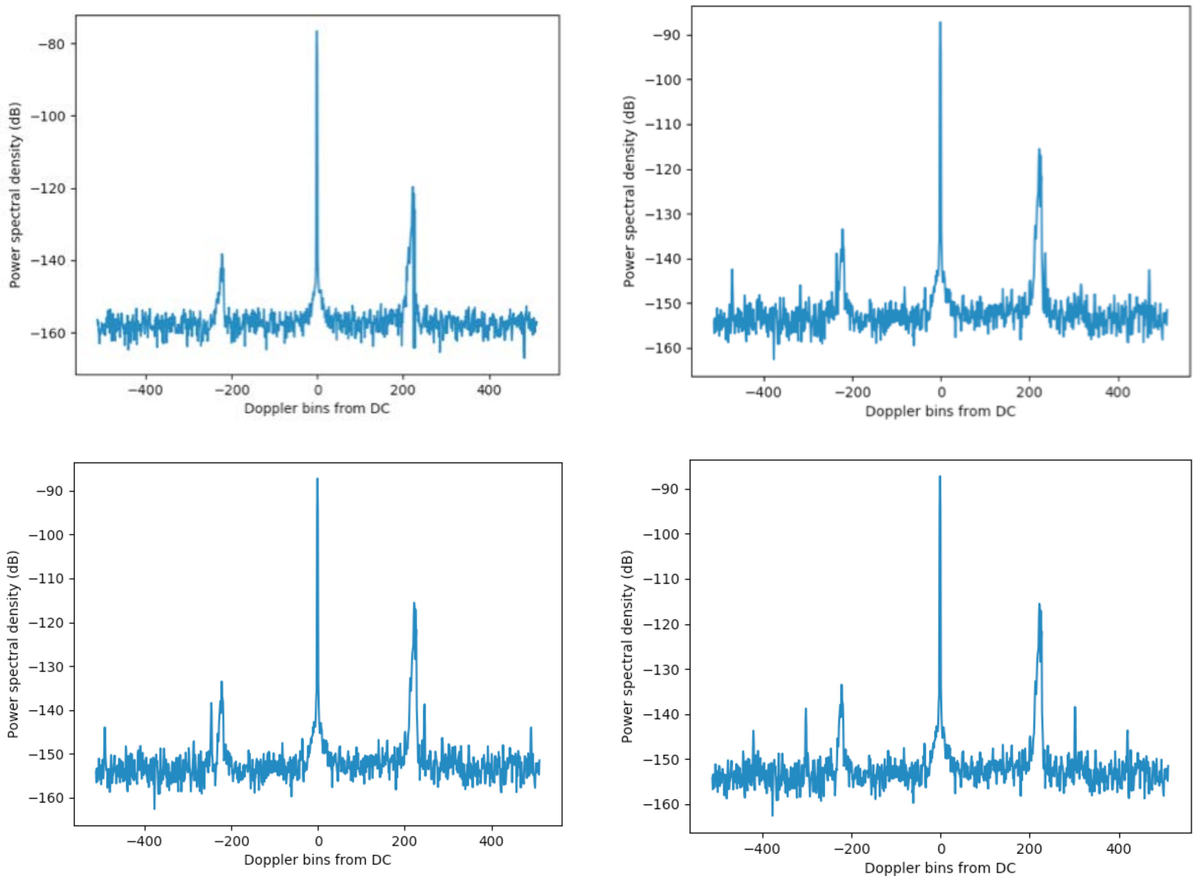

Figure 10. Simulated wind turbine interference added to SeaSonde cross-spectra.
Top Left: The first range cell from the original radar cross-spectra. Top Right: Modified cross-spectra after adding simulated wind turbine interference corresponding to a 0° nacelle angle and 4.6 RPM. Bottom Left: Modified cross-spectra after adding simulated wind turbine interference corresponding to a 0° nacelle angle and 4.8 RPM. Bottom Right: Modified cross-spectra after adding simulated wind turbine interference corresponding to a 0 degree nacelle angle and 5.9 RPM.

The wind turbine interference simulated with NEC must be scaled appropriately for each antenna before it is added to the wind turbine interference-free cross spectra. The scaling is first determined for antenna three, the monopole; then the ratios of each of the loop antennas (one and two) versus antenna three are determined using the measured antenna pattern for a predetermined bearing. To get a realistic scaling on antenna three, we chose seven cross-spectra from May 2017 during times for which we had a record of the rotation rates of the turbines and during which times the turbines were all rotating at approximately the same rate. With the rotation rates known we were able to use the results from Appendix B to identify the eight range-Doppler bins that would contain wind turbine interference. We then used the least squares method to fit the wind turbine interference simulated with NEC to the wind turbine interference on the antenna 3 self-spectra in eight impacted range-Doppler bins giving us the scaling function

$$WTI_s = (8.91e-13)WTI_{nec} + 3.82e-12\,, \qquad (0.6)$$

where WTI_{nec} is the wind turbine interference simulated with NEC, and WTI_s is the scaled interference ready to be added to the cross spectra.

Recall that the scaling function was fit to data when all five turbines were operating. For simulations looking at the impact of a single wind turbine, we divided WTI_s by five before adding it to the cross-spectra. In Figure 16 we show three examples of the signal in the first range bin of the cross spectra before and after the simulated wind turbine interference is added.

C.3 Video Processing

In the following sections, we show the dependence of the wind turbine interference impact on the rotation rates. Furthermore, the rotation rates are necessary to calibrate the simulated wind turbine interference, as explained in the previous section, as well as investigate the likelihood of an impact. The wind turbine rotation rates and nacelle angles are dynamic parameters and are not given in any source. Cameras were installed at the Southwest lighthouse on November 14th 2016, to obtain the rotation rate of each of the five wind turbines. A Python script was used to extract the rotation rate of each of the five turbines from the video feed. An overview of the method used to extract the rotation rates and nacelle angles from the video is found Appendix F.

C.4 Impacts On Ocean Current Measurements

Sea surface current measurements are the most common use of coastal oceanographic HF radars. The current data are used for a variety of things such as search and rescue and oil spill response. The region in range-Doppler space of the cross-spectra that contains the sea echo is called the Bragg region. In the plot shown in Figure 18, the Bragg region is outlined in white. For each range cell, the Bragg region contains the sea echo at Doppler velocities equal to the sum of the ocean current and the Bragg wave phase velocity, where the Bragg waves are ocean waves that are half the wavelength of the radar wave. The spread in the Bragg regions is due to the presence of fluctuating currents. For each cross-spectra, there are two Bragg regions, one on the positive side of the Doppler Spectrum and the other on the negative side, corresponding to Bragg waves moving towards the radar and away respectively. A direction finding algorithm is applied to each range-Doppler bin in the Bragg region to obtain a radial current vector. The radial current vectors contain the component of the current velocity component towards the radar. If the boundaries of the Bragg regions are incorrectly defined then erroneous radial current vectors are produced.

In this section, we show how wind turbine interference impacts quality of the current measurements by either shifting the boundaries of the Bragg region when the interference is found near the Bragg region boundaries or by changing the velocity vectors when the wind turbine interference is contained within the Bragg region.

Each of the 1463 cross-spectra with simulated wind turbine interference was reprocessed using SeaSonde software to obtain the boundaries of the Bragg region as well as the radial current, to investigate the impacts of wind turbine interference. The reprocessed radial currents and Bragg regions are compared to the radial currents and Bragg boundaries from the original wind turbine interference-free cross-spectra. We observe that, for a single turbine, the wind turbine interference only impacts, at most, the four range cells before and after the range cell containing the wind turbine. At BLCK the wind turbines are located precisely in the first range bin, limiting the impact of the wind turbine interference to the first five range bins. Thus, we limit analysis to the first five range bins.

C.4.1 Wind Turbine Interference Outside the Bragg Region

As established above, an essential task of the SeaSonde backscatter cross spectra processing is identifying the boundaries of the Bragg regions also referred to as the first order region. The boundaries of the first order region are called the first order lines (FOL). To obtain accurate ocean currents, the FOL must be chosen correctly. The algorithm that defines the FOL treats each range cell independently. After smoothing the spectrum in a range cell, the FOL algorithm calculates the noise floor using the values in the Doppler bins near the edges of the spectra. The noise floor is used as a threshold and to identify the nulls of the Bragg region. Usually, the Bragg region is separated from other signal sources in the spectra by these well-defined nulls. The algorithm tries to identify the null and place the FOL at the nulls. Thus, wind turbine interference can change the FOL locations by either changing the calculated value of the noise floor or by changing the detectable location of the nulls.

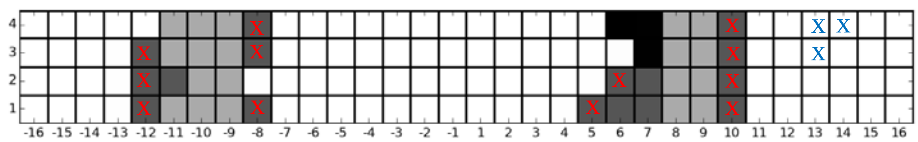

Figure 11. Example of the locations of wind turbine interference peaks.
Light gray and black bins show which range-Doppler bins would be in the Bragg region in the absence of turbine interference. Dark gray bins represent bins that would be added due to turbine interference and the black bins are those that would be removed as a result of the presence of turbine interference. The bins containing wind turbine interference are marked with an X.

To illustrate the two ways wind turbine interference changes the boundary determination of the Bragg region, consider the simplified depiction in Figure 17. To be consistent with SeaSonde cross-spectra the horizontal axis in Figure 17 represents the Doppler bin and the vertical axis the range bin. The range-Doppler bins containing wind turbine interference are demarcated with an X. The light gray and black bins show the bins that correctly belong to the Bragg region, while the dark gray bins are range-Doppler bins that have been added to the Bragg region as a result of the wind turbine interference. The black bins are bins that have been removed from the Bragg region result of the wind turbine interference. When the wind turbine interference is near the correct Bragg boundaries, as with the bins marked with a red X, the FOL are shifted to include the wind turbine interference, resulting in the addition of the dark gray bins to the Bragg regions. In contrast, if the interference is found near the edges of the spectra, bins marked with a blue x, then the noise floor is set to high and bins can be removed, as it is for range cells 3 and 4.

We use the simulated cross-spectra to assess the impact of shifting the FOL. Working with the twelve wind turbine interference-free cross-spectra from spring and summer 2016, we generate cross-spectra with simulated wind turbine interference for the 1,463 combinations of RPM and nacelle angle mentioned above. The FOL and radial currents were then extracted from each of the simulated cross-spectra as well as for the original wind turbine interference-free cross-spectra. By analyzing the four FOL boundaries of the simulated cross-spectra and comparing them with the corresponding original files (before adding turbine interference) we observe which combinations of RPM and nacelle angle represent a bigger error in the FOL determination. In Figure 18 we show examples of how wind turbine interference shifted the calculated Bragg regions. The top plot gives the Bragg regions in the absence of wind turbine interference and the middle and bottom plots show how the Bragg region can grow or shrink, respectively, as a result of wind turbine interference.

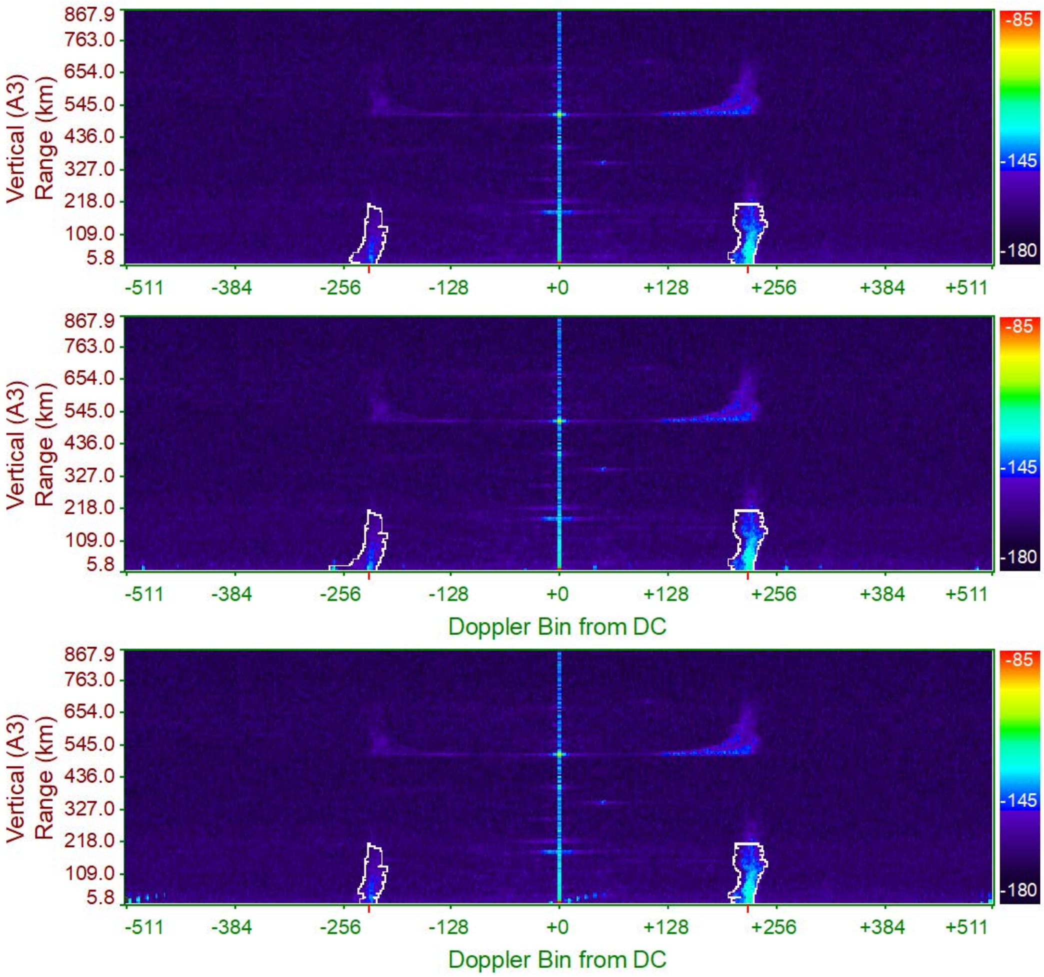

Figure 12. Antenna three self-spectra.
No wind turbine interference (top); wind turbine interference near the original FOL (middle); wind turbine interference near the edge of the spectra (bottom).

Looking at the range slice of the cross-spectra, we can see both types of FOL errors in more detail. In Figure 19 we compare the Doppler spectra of the first range cell with and without wind turbine interference. The top plot of Figure 19 has no wind turbine interference and shows the location of the four FOL with light blue vertical lines. The bottom plot shows the FOL after the addition wind turbine interference corresponding to a wind turbine spinning at a 5.2 RPM and with a nacelle angle of 15°. The wind turbine interference peak near the left boundary of the negative Bragg region has caused the FOL algorithm to shift the location of the Bragg region boundary to the left by 37 Doppler bins to include the interference peak. The shift of the FOL adds or changes the value of multiple radial current vectors. We plot the radial currents in the first range bin for both cases in Figure 22. Comparing the resulting current maps in Figure 22 we observe several new current vectors that have been added or changed as a result of the wind turbine interference. The velocity vectors with a magnitude near 100 cm/s in the first range cell of the middle plot of Figure 22 correspond to the wind turbine interference peaks added to the Bragg region.

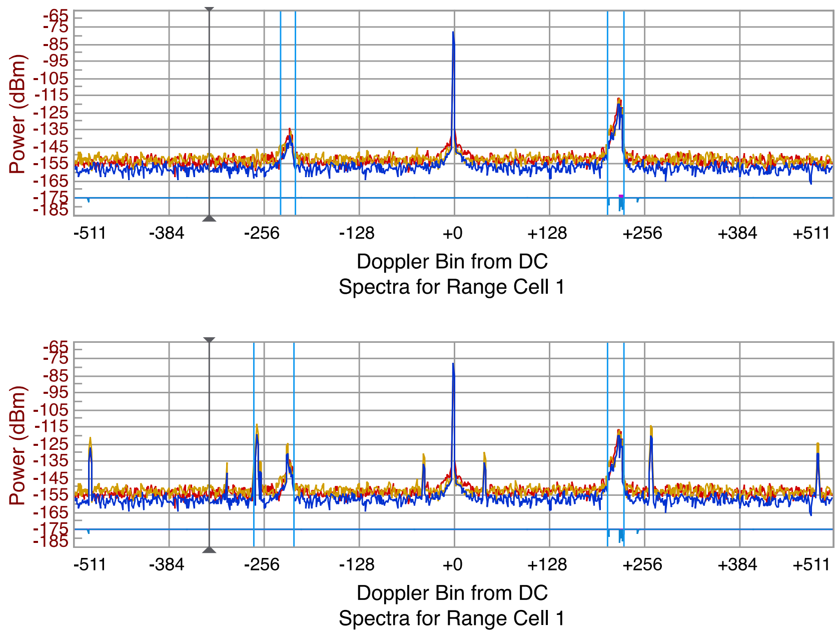

Figure 13. FOL determination in range cell one.
Cross-spectra with wind turbine interference (bottom) and without wind turbine interference (top). The wind turbine interference corresponds to a turbine spinning at 5.2 RPM with a nacelle angle of 15°. The FOL are marked with vertical blue lines. The wind turbine interference is near the original Bragg region, resulting in a shift of the leftmost FOL to include some of the wind turbine interference.

Using the simulations, we also demonstrate how the Bragg regions can shrink as a result of wind turbine interference. In Figure 20 we compare the Doppler spectra of the third range cell with and without wind turbine interference. The top plot of Figure 20 has no wind turbine interference and shows the location of the four FOL in blue. The bottom plot shows the FOL after the addition of wind turbine interference corresponding to a wind turbine spinning at a 10.4 RPM and with a nacelle angle of 70°. In this case, the three wind turbine interference peaks near the left side of the spectrum have caused the FOL algorithm to overestimate the noise floor, and the location of the leftmost FOL is shifted right removing 17 Doppler bins. The shift of the FOL results in the loss of current measurements. The radial currents in the first range bins for both cases are displayed in the top and bottom plots of Figure 22. Comparing the resulting current maps in Figure 22, we observe the lost several current vectors in the first range bins. The shift removes the velocity vectors with the strongest velocities.

The locations of the wind turbine interference peaks are functions of the rotation rate, and the amplitudes of the peaks are functions of the nacelle angle. Using the 1463 combinations of RPM and nacelle angle for each of the twelve files we can see the shifts in the FOL caused by the wind turbine interference. The left plot of Figure 21 shows the average, across the twelve files, number of range-Doppler bins added to the Bragg regions for each rotation rate. Figure 21 shows that while there are relatively few RPM that add more than 10 bins to the Bragg region, there are even less RPM that have no impact on the FOL locations. Thus, the current measurements will be impacted for almost all rotation rates of an operational wind turbine.

As we demonstrated above in addition to adding range-Doppler bins to the Bragg region, bins can also be removed if there is sufficient wind turbine interference near the edges of the spectrum. The plot on the right side of Figure 21 shows the average number of bins lost from the Bragg regions for each rotation rate and nacelle angle. When turbines are rotating at 5 or 10 RPM, all the turbine interference peaks are located in the Doppler bins on the edge of the range cells and at zero Doppler, resulting in no impact to the Bragg region. However, as the rotation rates increase or decrease slightly the interference peaks spread out quickly along the edges of the range cells, as shown in Figure 20, causing the noise floor to be overestimated and the Bragg regions to lose bins.

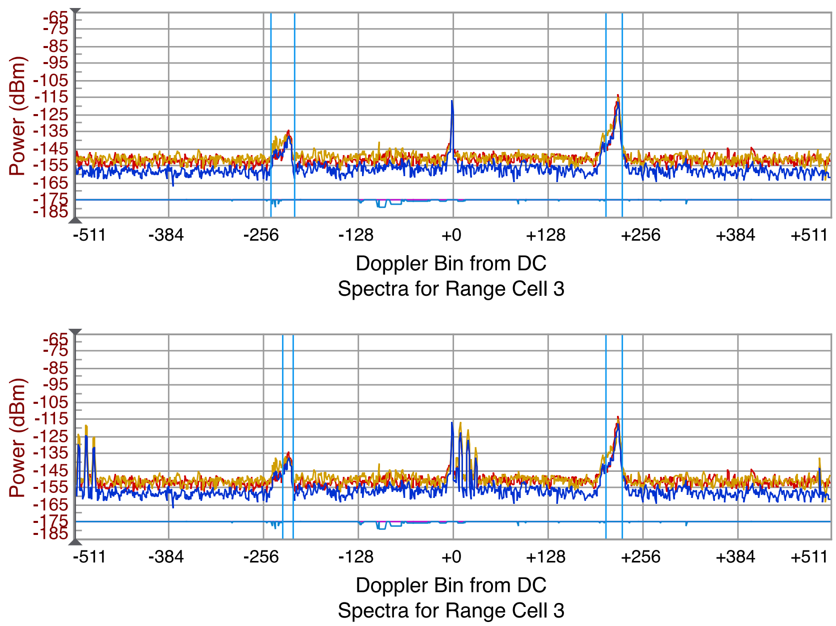

Figure 14. A comparison of FOL determination in range cell one.
Cross-spectra with wind turbine interference (bottom) and without wind turbine interference (top). The wind turbine interference corresponds to a turbine spinning at 10.4 RPM with a nacelle angle of 70°. The FOL are marked with vertical blue lines. The wind turbine interference is at the edge of the spectra, resulting in a higher noise floor calculation and a shrinking of the Bragg region.

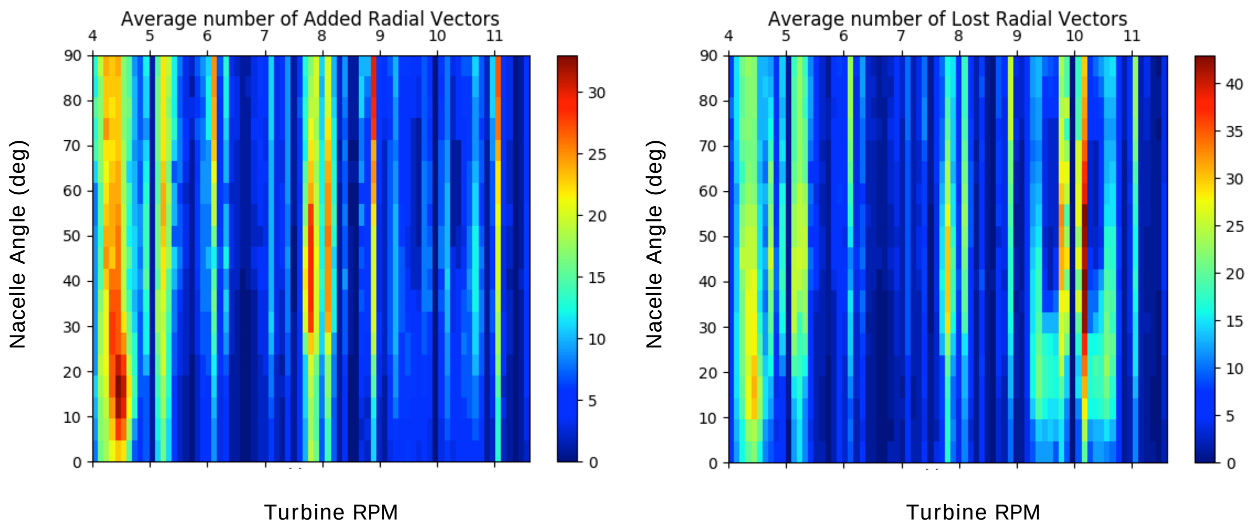

Figure 15. Changes in the number of range-Doppler bins included in the Bragg region.
The average number of bins added to the Bragg region (left) and the average number of bins lost from the Bragg region (right) for each nacelle angle and RPM.

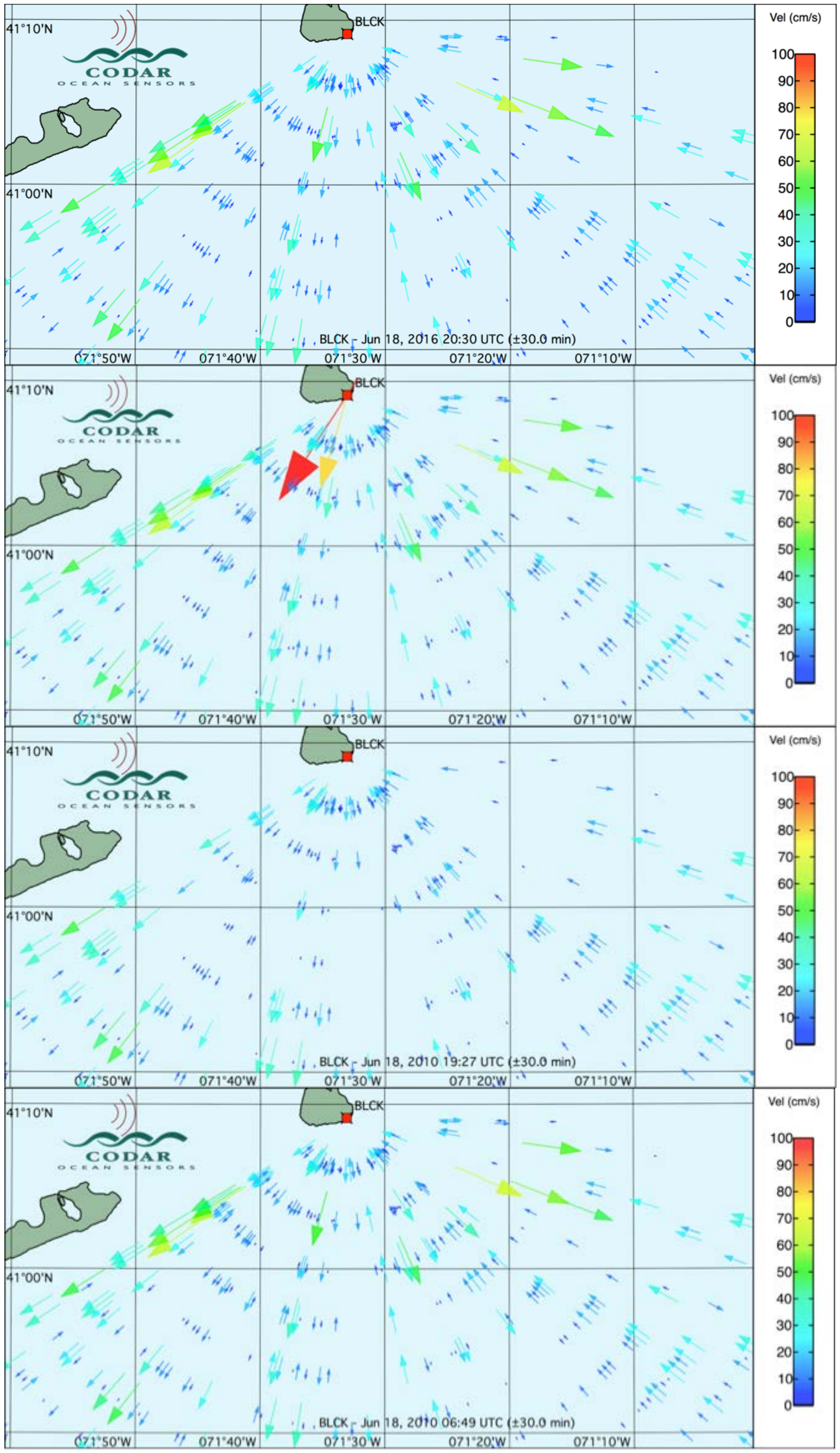

Figure 16. Radial current maps

No wind turbine interference (top); wind turbine interference near the original FOL (second from top); wind turbine interference near the edge of the spectra (second from the bottom); and wind turbine interference in the Bragg region (bottom).

C.4.2 Wind Turbine Interference Inside the Bragg Region

The other possibility is that some of the wind turbine interference peaks fall in the Bragg region. When the wind turbine interference is in the Bragg regions there is less impact, but the wind turbine interference is more difficult to detect. An example of the interference in the Bragg regions of the first range cell can be seen in Figure 23. When the wind turbine interference is in the Bragg region it is difficult to distinguish it from the sea echo. However, since it does not affect the location of the FOL fewer current vectors are changed. The wind turbine interference peaks in the Bragg region span at most three range-Doppler bins, limiting the impact to at most three radial vectors. The wind turbine interference changes the radial vector calculations either by changing velocity at a given bearing or by shifting the bearing determination, meaning the desired bearing will be misplaced to an erroneous bearing position, resulting in consequent errors in radial velocities.

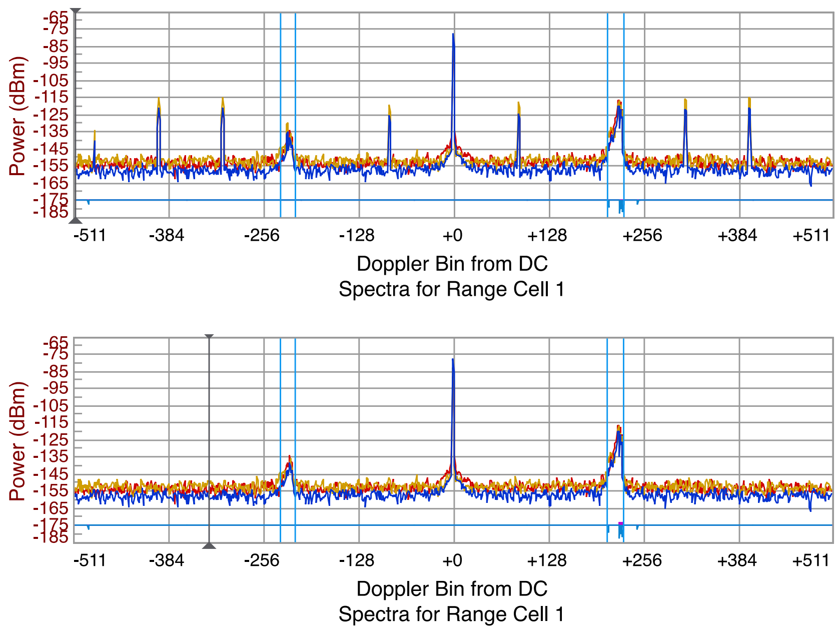

Figure 17. Impact of wind turbine interference on FOL determination.
A comparison of FOL determination in cross-spectra for range cell one, with wind turbine interference (bottom) and without wind turbine interference (top). The wind turbine interference corresponds to a turbine spinning at 6.1 RPM with a nacelle angle of 50. The FOL are marked with vertical blue lines. The wind turbine interference is closer to the edges of the spectra, resulting in a higher noise floor calculation and a shrinking of the Bragg region.

One of the tasks of the direction finding algorithm is to determine how many bearing solutions there are for a particular range-Doppler bin. SeaSonde radars have three antennas, which allows up to two bearing angles per range-Doppler bin. When a bin contains wind turbine interference the direction finding algorithm may determine that bins that previously had a dual-angle solution now have only one single-angle solution, which may even be different from either of the original dual-angle solutions. Alternatively, the wind turbine interference may also cause a single-angle solution to become a dual-angle solution. The result, in either case, is that the radial vector is assigned a new bearing.

In addition to shifting the bearing of a radial vector, wind turbine interference peaks in the Bragg region can also change the magnitude of the radial vectors. To understand how we must understand what the radial vector processing software does when multiple radial vectors are assigned to the same range and bearing. Often, after using the direction finding algorithm, multiple Doppler velocities are assigned to the same bearing and a decision must be made as to what radial velocity to assign to that location. The strategy used by the SeaSonde software is to average all the vectors together. wind turbine interference that create a new dual-angle solution or shift a radial vector to different bearing will, therefore, bias the average at the new location.

To assess how significant the impact of wind turbine interference peaks is in the Bragg region, we tracked the number of radial vectors that had their bearing angles changed. The results are plotted in Figure 24. As mentioned in the previous paragraph, this does not assess the total impact of the wind turbine interference in the Bragg region. However, when the wind turbine interference is outside the Bragg and the FOL are shifted, the radial vectors also change their magnitudes.

C.5 Impact

In the previous section, we showed that the impact a wind turbine has a dependency on its rotation rate. To solidify the rotation rate dependence, we averaged the total number of range-Doppler bins added to the Bragg region across all twelve files and all nacelle angles. We plot the results in Figure 25 with the blue line and show a standard deviation above and below in green.

Looking at both the right and the left of Figure 25 we see that RPMs having a low number of bins added, have a high number of bins lost and vice versa. This implies that there are very few rotation rates that do not affect the current measurements in the range cells near the turbine. As we see in the plot on the left-hand side of Figure 28, this is indeed the case.

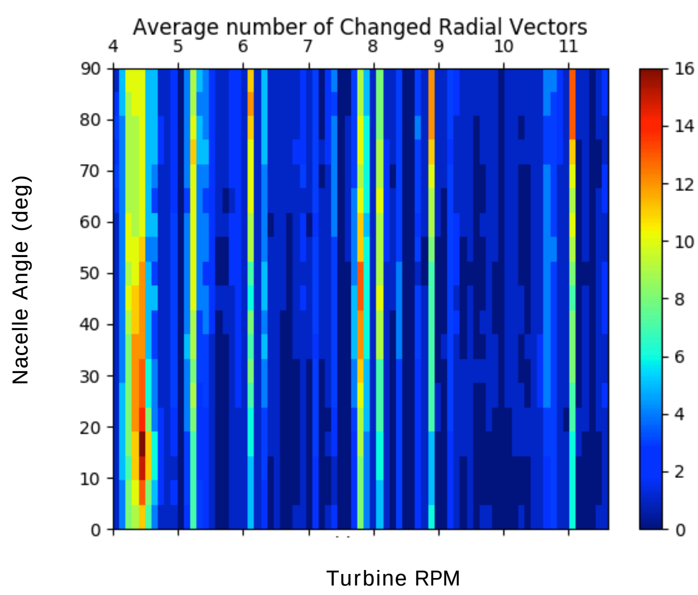

Figure 18. Average number of changed radial vectors

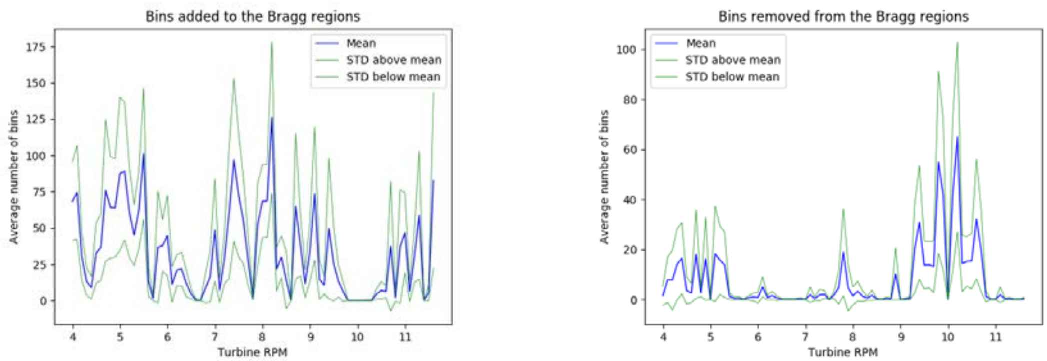

Figure 19. Changes in the number of bins in the Bragg region.
The Mean and standard deviation of the average number of bins that have been added (left) and removed (right) from the Bragg regions for each of the RPM.

The histogram on the left of Figure 26 shows the percentage of time the Bragg region was changed as a result of the wind turbine interference. The percentage was taken across all nacelle angle and all twelve files giving a total of 228 possibilities for each RPM.

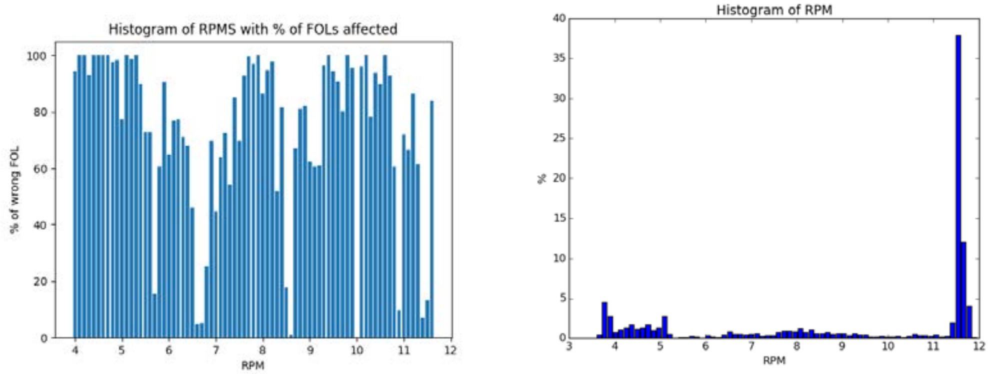

Figure 20. Histograms of the turbine rotation rates.
Left side is percent time turbines spend at a given rotation rate. Right plot is a histogram of the percent of observed rotation rates vs. RPM. For the observed period, most occurred near 11.5 RPM.

The turbine rotation rate, which is limited to 4–12 RPM at BLCK, does affect the impact of the wind turbine interference. However, the time a turbine spends at each rpm is not uniformly distributed. To understand what the RPM distribution looks like for the turbines at Block Island we collected videos from the month of November 2017 and tracked the rotation rates of each of the turbines as outlined above. It should be noted that we did not collect data for turbines that were not rotating. Furthermore, it was not possible to collect data from every video, as the turbines were not always visible.

We have plotted the percentage of time the turbines spend at each rotation rate in the histogram on the right-hand side of Figure 26. The turbines spent most of their time around 11.5 RPM, which is not a rotation rate that places interference in the Bragg region. Furthermore, while it was observed in the simulations that the Bragg regions are changed at 11.5 RPM the total number of bins added and lost is fewer than five. Thus, the impact of an 11.5 RPM is not significant.

C.6 Frequency and Range dependence

In addition to RPM and nacelle angle, we know that both the frequency of the turbine and range to the turbine also change the impact of the wind turbine interference. As with the sea echo, the wind turbine interference impact drops off quicker at higher radar frequency. However, this is not the only impact the frequency has on the severity of the wind turbine interference. In Figure 12 we plot the energy in each of the first four positive and negative Fourier harmonic modes of the radar cross-section over 120° interval of rotation, the periodic interval for three-blade turbines. The energy in each of the harmonics is plotted as a function of the nacelle angle, varying from 0° to 90°. Recall that each of the harmonics maps to a single interference peak in the cross-spectra, the amplitude of which is proportional to the amplitude of the RCS harmonic. From Figure 12 we see that at higher a frequency, the portion of nacelle angles for which the harmonic modes have significant energy is reduced; reducing the portion of nacelle angles that produce wind turbine interference above the noise floor in the spectra.

At 5 MHz there is sufficient energy in at least one mode for all nacelle angles; however, at 25 MHz the window of significant nacelle angles is limited to 2–12, and even then it is limited to the first few harmonic modes. This agrees with our observations at Block Island where there are both 5 MHz (BLCK) and 25 MHz (BISL) radars installed 5 km from the wind turbines. There are very few times when the wind turbine interference is observable on the 25 MHz radar. In contrast, when the turbines are operating, they are almost always observable on the 5 MHz radar. An example of a time when the wind turbine interference is observable on the 25 MHz radar is shown in Figure 28, where one of the interference peaks detected is at the BISL Block Island site. Note that in this case, the wind turbine interference appears in the fourth range bin instead of the first as it does at BLCK due to the higher range resolution at higher radar frequencies.

While the Block Island wind farm is a great test bed to investigate the characteristics and impact of the wind turbine interference, it has not proved suitable to investigate with any rigor the impact of the distance between the turbine and the SeaSonde. The wind turbines in the Block Island wind farm are all in the same range bin so we could not measure the range attenuation. For the same reason, we could not use simulations, as we have no way to infer the range attenuation factor.

While we are unable to measure the range attenuation of the turbines, we do know that it is proportional to $1/R^4$ while the sea echo is reduced by a factor of $1/R^3$. Thus, the signal of the wind turbine falls by a factor of $1/R$ faster than the sea echo due to the expanding range cell in bearing angle. This helps explain why the wind turbine interference is not visible on any of the other 25 MHz radars even as close as 30 km. However, we have detected noticeable wind turbine interference at MVCO radar, see Figure 29, which operates at 5 MHz, where we detect the strongest interference of the MVCO radar in range bin 16 and at Doppler bin -436 from DC.

The wind turbine interference clearly drops off with range but further study must be done to properly model the signal at arbitrary ranges. Furthermore, the attenuation is expected to change somewhat from radar to radar.

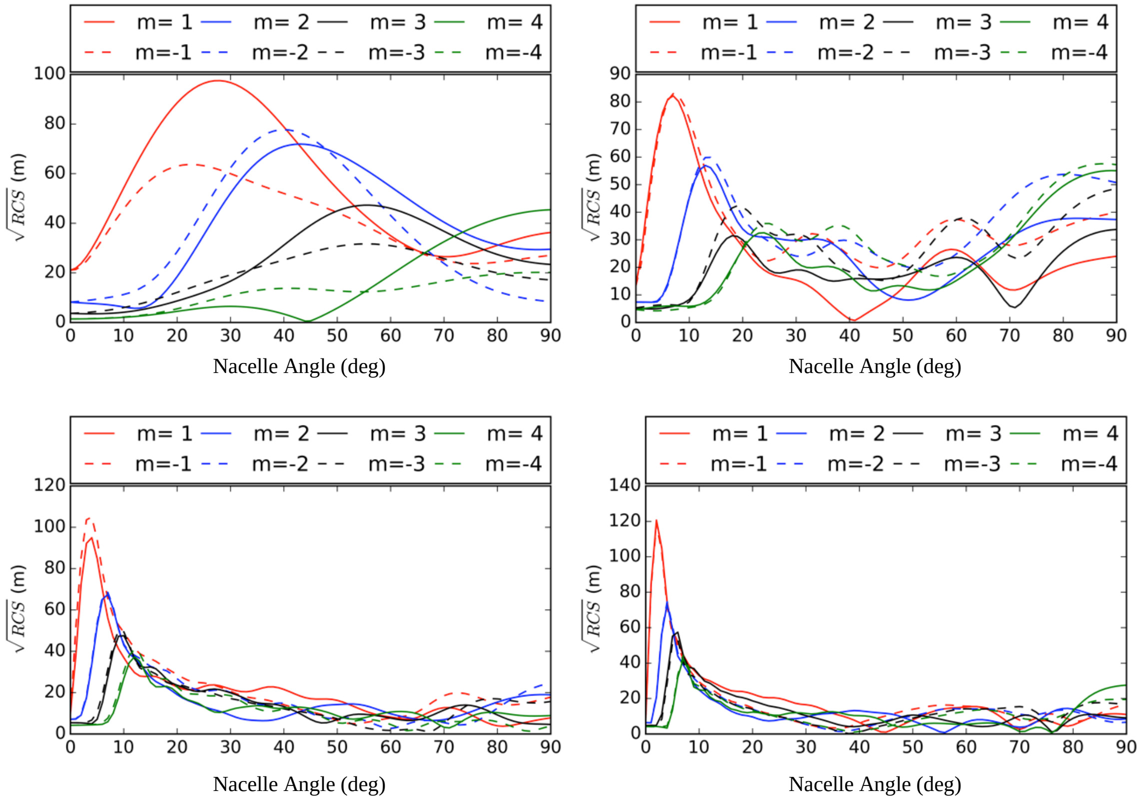

Figure 21. Amplitude coefficients of the first four positive and negative harmonics.
The dependency of the amplitude coefficients of the first four positive and negative harmonics on nacelle angle at 4.538 MHz (top left), 13 MHz (top right), 25 MHz (bottom left), and 42 MHz (bottom right).

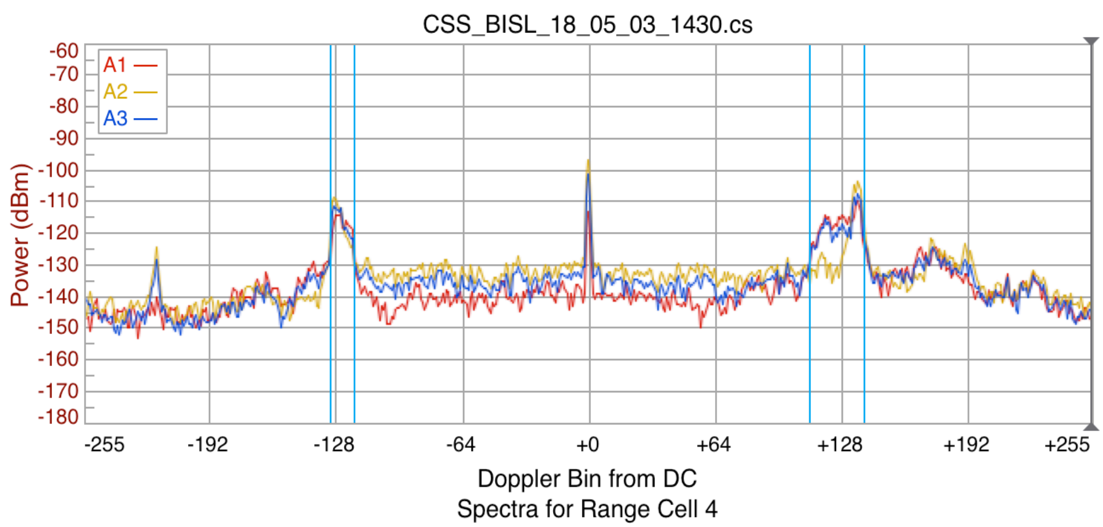

Figure 22. Wind turbine interference at 25 MHz.
512-sample sea echo power spectrum recorded by 25 MHz BISL radar on May 3 2018, 14:30 UTC.

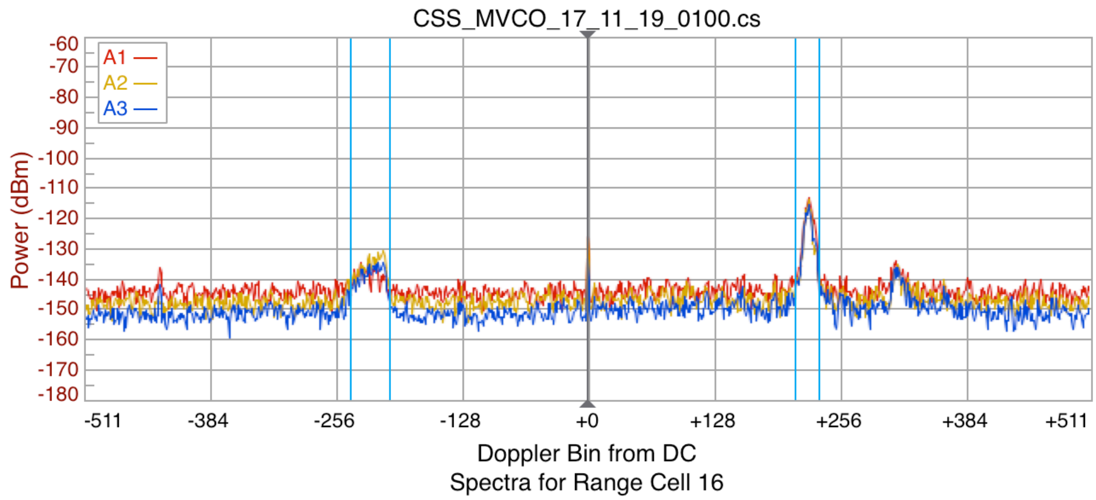

Figure 23. Wind turbine interference at 5 MHz.
1024-sample sea echo power spectra at MVCO 5 MHz radar on November 11 2017, 1:00 UTC.

C.7 Conclusion

CODAR has demonstrated that the existence of offshore turbines, like the five present in the Block Island Wind Farm, produces interference in oceanographic HFR Doppler spectrum that impacts the surface current map products. The impacts have been shown to manifest in three key ways when turbine echoes are present in the Doppler spectrum: biasing the measurement of the true background noise level (affecting the sea echo identification algorithms), changing the boundaries of the sea echo peaks by mischaracterizing turbine echoes as part of the sea echo, or changing the bearing assignment to the radial current vectors by causing turbine echoes to be convolved within the sea echo. While each of these impacts occur under different but overlapping combinations of conditions, we observe that one or more of them occurring at all can result in errors in the velocity measurements up to 48 cm/s and, thus, reduce the accuracy and effectiveness of the data being supplied to responders for spill response, search and rescue and the various other applications identified for HFR data products.

This Appendix describes the findings using real HFR Doppler spectra from the Block Island Wind Farm with turbine echoes present and, more importantly, spectra obtained prior to turbine installation that have had simulated turbine echoes added to measure the impact in a controlled manner. These simulations have been validated against the real time data being collected now. The nature of the Block Island Wind Farm, containing only five sites and oriented in an arc around the existing HFR stations, was beneficial for isolating the effects from a small number of turbines and allowed CODAR engineers to discover an analytical, closed-form solution for the Doppler frequency and relative amplitude of turbine peaks and harmonics as a function of turbine position, RPM and nacelle angle. The impacts detailed here are necessarily specific to the Block Island configuration for validation and comparison, but the general results can be extended to other configurations using the analytical solution developed. Under an increased scope of work, an investigation of the impacts on HFR from the larger wind farms being planned can be studied. In addition to describing the impacts, the analytical solution for turbine peak Doppler frequency and amplitude also form the basis for the mitigation techniques described in Appendix D.

Appendix D: Wind Turbine Interference Mitigation

In Appendix B, CODAR demonstrated the ability to predict the location of wind turbine interference in the Doppler spectrum given the rotation rate of a wind turbine. It was shown that wind turbine interference is a result of the amplitude modulation of the radar cross-section (RCS) of a rotating wind turbine. Furthermore, it was shown that each of the harmonic components of a 120° period of the rotating turbines' RCS introduces wind turbine interference in a single range-Doppler bin in the SeaSonde cross-spectra. However, in practice, only the first four positive and negative harmonics have enough energy to be above the noise floor for the 5 MHz radar band; thus for a single wind turbine, there are at most eight wind turbine interference peaks in the cross-spectra. In Appendix B, equations were derived giving the range-Doppler bin corresponding to each of the harmonic modes as a function of the rotation rate.

Following Appendix B, CODAR utilized a series of numerical simulations and observations in Appendix C, to show the different ways that the existence of offshore turbines, like the five present in the Block Island Wind Farm, produce interference in oceanographic high-frequency radar (HFR) Doppler spectrum that impacts the surface current map products. The impacts have been shown to manifest in three fundamental ways when turbine echoes are present in the Doppler spectrum:

- biasing the measurement of the actual background noise level (affecting the Bragg sea echo peak identification algorithms)
- changing the boundaries of the sea echo peaks by mischaracterizing turbine echoes as part of the sea echo
- changing the bearing assignment of the radial current vectors by causing turbine echoes to be convolved within the Bragg sea echo peaks

In this Appendix, we focus on wind turbine interference mitigation techniques. We develop and test three different types of filters designed to isolate and mitigate each of the three types of impacts identified in Appendix C. We then test different combinations of the filters to assess their effectiveness at mitigating both simulated and measured wind turbine interference from SeaSonde cross-spectra.

To locate wind turbine interference in the Bragg regions, we first estimate the rotation rates of the wind turbines from spectral peaks outside of the Bragg region. The equations derived in Appendix Bare then used to identify and tag the range-Doppler bins in the Bragg region that contain wind turbine interference.

The remainder of this Appendix is organized as follows: We start with an explanation of each of the filters used to construct the different mitigation algorithms. Following the explanation of the filters, we present an outline of the six mitigation algorithms that we test along with the mitigation assessment methods. We conclude with a discussion of the benefits and weakness of each of the methods along with suggestions for future work.

NOTE: Appendix D content is proprietary and will be provided with permission on request.

Appendix E: FMCW Waveform Processing

E.1 Transmitted Waveform

The frequency modulated waveform of a SeaSonde radar can be expressed as a saw tooth function

$$f = f_c + B(t \bmod T), \qquad (0.7)$$

where f_c is the carrier frequency, B is the bandwidth, t is the time in seconds, and T is the time in seconds to complete a sweep. We have plotted the Frequency as function of time in Figure 35.

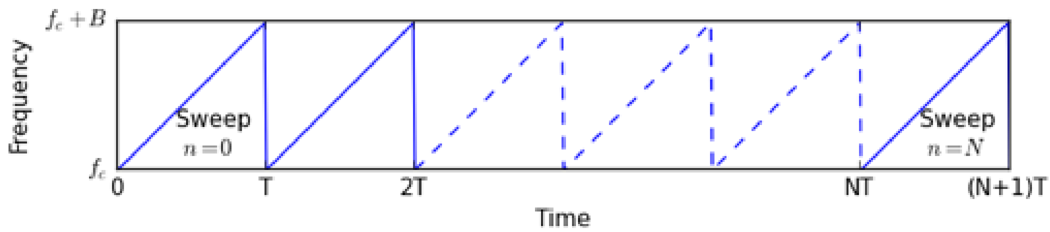

Figure 24. Frequency of the transmitted wave.

Since the derivative of the phase is equal to the frequency, the expression for the complex transmitted wave is written as

$$v_x(t) = c_0 e^{2\pi i\left(f_c t + \frac{B(t \bmod T)^2}{2T}\right)}, \qquad (0.8)$$

where we have used c_0 as an arbitrary amplitude coefficient. Letting n represent the sweep number we can rewrite (0.33) as

$$v_x(t) = c_0 e^{2\pi i\left(f_c t + \frac{B(t-nT)^2}{2T}\right)}. \qquad (0.9)$$

E.2 Returned Signal From a Stationary Hard Target

When the EM wave reflects off a hard target at a distance R from the transmit/receive antenna moving with a velocity V towards the receiver, the amplitude of the signal at the receiver is proportional to the product of the RCS and $\frac{1}{R^2}$.

Furthermore, the waveform remains the same only delayed by the travel time of the EM wave. The travel time, t_d, is a function of the distance between the radar and the target, the target velocity, and the speed of light, c,

$$t_d = \frac{2R}{c}. \qquad (0.10)$$

If we let $\alpha(t)$ represent the radar cross section of the target at time *t*, we can then write the equation of the received signal as

$$v_r(t) = \frac{c_0}{R^2}\alpha(t - \frac{t_d}{2})e^{-2\pi i\left(f_c(t-t_d)+\frac{B(t-t_d-nT)}{2T}\right)}, \tag{0.11}$$

where we have absorbed all proportionality constants into c_0.

E.3 Mixed Signal

To obtain the mixed signal we multiply the received signal and the transmitted signal to get

$$v_{mix}^{m}(t) = \frac{c_0\alpha(t - \frac{t_d}{2})}{R^2}e^{2\pi i\left(f_c(t-t_d)+\frac{B(t-td-nT)}{2T}\right)}e^{2\pi i\left(-f_c t+\frac{B(t-nT)}{2T}\right)}. \tag{0.12}$$

Next we make the substitutions $t = t' + nT$ and $t_d = \frac{2R}{c}$ into equation (0.37), then we remove any terms, which are quadratic in t', and simplify to get

$$v_{mix}^{m}(t') = \frac{c_0}{R^2}\alpha\left(\frac{1}{c}((t'+nT)(1-V)-R)\right)e^{2\pi i\left(f_p t'+f_D T\right)}, \tag{0.13}$$

where $f_D = \frac{2f_cV}{c}$ and $f_p = \frac{2BR}{cT} + f_D + \frac{2BnV}{c}$.

Appendix F: Rotation Rate Measurements

The wind turbine rotation rates and nacelle angles are dynamic parameters and are not available from the turbine manufacturers or operators. To obtain the rotation rate of each of the five wind turbines, we installed cameras at the Southwest light house on November 14th 2016. A script was written to extract the rotation rate of each of the five turbines from the video feed. Below we outline the method used to extract the rotation rate of the turbines.

The basic outline of the method is as follows:

- Get the blade positions and the nacelle angle of each turbine;
- Estimate the RPM using a Kalman filter;
- Use machine learning to remove erroneous data segments.

F.1 Blade Position and nacelle angle

The time scale at which the background in each frame of the video changes is much slower than the rate at which the turbine blades are rotating. This suggests the application of a background subtraction method to find the turbine blades in each frame. For each turbine, the blade position, ϕ, the method is outlined as follows:

1. Crop a small region containing the turbines
2. Subtract the background
3. Use reference images to estimate the blade positions and the nacelle angle

This process is repeated for each frame giving a time series of blade positions, which are used to calculate rotation rate. All image processing was done using Python and OpenCV (Bradski 2000).

F.1.1 Step 1: Crop a small region containing the turbines

To determine the region of interest containing the turbine, the user inputs the center and radius of the turbine fan blades. The box is centered on the turbine fan that is one and a half times the diameter of the fan; this is the used to crop the image of the turbines. This cropped image is then used in the remainder of the steps to reduce the computational time.

F.1.2 Step 2: Subtract the background

The background was subtracted using the method proposed by (KaewTraKulPong and Bowden 2002) and implemented in OpenCV using five frames. The background represents all the stationary components in the video and remains relatively constant from frame to frame compared to the blade rotation rate. Since the blades are rotating they will not be part of the background and will remain once it has been subtracted. The output of the background subtractor is a binary image, the same size as the input image, where the foreground pixels—the pixels corresponding to the blades and other noise—are white. The noise is reduced by the application of an erosion followed by a dilation.

F.1.3 Step 3: Use reference images to estimate the blade positions and the nacelle angle

The final step is to determine the blade position and nacelle angle of the turbine. A set of binary reference images is created using a turbine model with the blade at different rotation angles and nacelle angles.

Then we varied the rotation angle from 0° to 120° in 0.5 increments and varied the nacelle angle from -90° to 90° in 1° increments. Each of the reference images is compared with the binary image obtained from the background subtractor. The reference image with the smallest mean square error is used to determine ϕ and the nacelle angle.

The rotation angles of the five matched reference images are recorded as the rotation angles for the turbines in the frame. Figure 36 shows one frame with all the strongest reference images superimposed in yellow on top of the blades.

F.2 Estimate RPM

Once the rotation angles are known they are filtered and used to generate a rotation rate using a Kalman filter. The Kalman filter reduces the error from measurement-to-measurement by utilizing time history of the measurements, while simultaneously using

$$\phi = RPM\frac{360}{60} + c \text{ , and} \tag{0.14}$$

$$RPM = \frac{d\phi}{dt}\frac{60}{360} \tag{0.15}$$

to obtain the rotation rate, where ϕ is the rotation angle of the turbine blades.

Figure 25. Image of the turbines from the nest camera.
The image was taken on 11/28/2016 at 12:00 pm EST. The blade positions are estimated and shaded yellow for visual confirmation.

We will give a brief outline of the main steps involved with the Kalman filter; for further details see (Challa, et al. 2011).

1. Compute the predicted state of the turbine given the state at the previous time step.
2. Calculate the predicted measurement, innovation co-variance matrix, and Kalman gain.
3. Compute the posterior mean and co-variance matrix using the difference between the measurement and predicted measurement.

The Kalman filter works by tracking the probability distribution of the state of the turbines through time. All variables are assumed to be normally distributed, and as such the mean and covariance of the turbine state are tracked through time. We let $x_k = [RPM_k, \phi_k, B_k]$ represent the state of the turbine, with RPM_k, ϕ_k, and B_k representing the RPM, angle of rotation of the fan, and the nacelle angle of the turbine at time k. Furthermore, we let P_k represent the covariance of the state vector at time k. We define the measurement vector at time k to be $z_k = [\phi_k, B_k]$ and assume the covariance of the measurement is constant in time (though this is not necessary), and represent it with R. We assume the turbine is rotating at a constant rate with an error that is normally distributed with ZERO mean and covariance Q.

F.2.1 Step 1: Compute the predicted state of the turbine

Thus, given x_k, we can then predict the state of the turbine, $\tilde{x}_{k+1}$, at time $k+1$, Δt seconds later, using

$$\tilde{x}_{k+1} = F_k x_k \text{, and} \tag{0.16}$$

$$\tilde{P}_{k+1} = F_k P_k F_k^T + Q, \tag{0.17}$$

where T is used for the transpose operator and the state update matrix is given by

$$F_k = \begin{pmatrix} 1 & 0 & 0 \\ \Delta t \dfrac{360}{60} & 1 & 0 \\ 0 & 0 & 1 \end{pmatrix}. \tag{0.18}$$

F.2.2 Step 2: Calculate the predicted measurement, innovation co-variance matrix, and Kalman gain

The transformation matrix from state to measurement space is defined as

$$H = \begin{pmatrix} 0 & 1 & 0 \\ 0 & 0 & 1 \end{pmatrix}. \tag{0.19}$$

Using $\boldsymbol{H}$ we can obtain our predicted measurement vector $\tilde{z}_{k+1}$, innovation co-variance $\tilde{S}_{k+1}$, and Kalman gain $\boldsymbol{K_{k+1}}$ with

$$\tilde{z}_{k+1} = H\tilde{x}_{k+1} \ , \tag{0.20}$$

$$\tilde{S}_{k+1} = H\tilde{P}_{k+1}H^T + R \ \text{, and} \tag{0.21}$$

$$K_{k+1} = \tilde{P}_{k+1}H^T\tilde{S}_{k+1} \ . \tag{0.22}$$

F.2.3 Step 3: Compute the posterior mean and co-variance matrix

We now correct the predicted state vector using the measurement from time $\boldsymbol{k+1}$ to obtain our final estimate for $\boldsymbol{x_{k+1}}$ and $\boldsymbol{P_{k+1}}$ using,

$$x_{k+1} = \tilde{x}_{k+1} + K_{k+1}(z_{k+1} - \tilde{z}_{k+1}) \ \text{, and} \tag{0.23}$$

$$P_{k+1} = \tilde{P}_{k+1} - K_{k+1}H\tilde{P}_{k+1} \ . \tag{0.24}$$

F.3 Filtering

There are times when the background is changing on the same time scale as the rotating blades due to the movement of clouds or other objects in the foreground. When this happens, the above algorithm fails to get a correct measurement of the blade positions. This can occur when birds, boats, people, etc. fly or pass through the frame or if the clouds near the horizon are varied and moving. To remove the erroneous vectors we split the time series using a change point detection algorithm (Killick et al. 2011) (Killick and Eckley 2014) (Killick and Eckley 2016).

Appendix G: RPM Estimation from Cross-Spectra

In this appendix we outline the method we use to predict the rotation rates of set, $W = (w_1, \ldots, w_n)$, of n turbines. It is assumed that each turbine is facing into the wind and that the wind is coming form the same direction at each turbine. Furthermore, we assume we have a fine set $R = (r_1, \ldots, r_m)$ of m possible rotation rates containing at least the rotation rates of each of the turbines. The estimation method is done using SeaSonde cross-spectra.

To get the best estimate of the nacelle angle and the rotation rates for each turbine we loop through every possible assignment of rotation rates from R to wind turbines in W and nacelle angles. Using equations (0.30) and (0.31) we can get the set s of range-Doppler bins that contain wind turbine interference in the cross-spectra. Each of the bins in s corresponds to one harmonic mode of the RCS. The amplitude of the wind turbine interference at each location is proportional to the amplitude of the harmonic mode of the RCS over the relevant 120˚ period of rotation.

Using the bins in s we form two comparison vectors $\overrightarrow{cs}$ and $\overrightarrow{nec}$. The first, $\overrightarrow{cs}$, is constructed from the values of the measured Antenna 3 self-spectra at each bin in s. The second, $\overrightarrow{nec}$, is formed from the amplitudes of the harmonic modes, corresponding to the bins in s, of the RCS estimated with NEC.

The values of $\overrightarrow{nec}$ corresponding to values of $\overrightarrow{cs}$ above the noise floor are used to calculate r_1, the correlation between the two vectors as well as to compute the scaling function which is applied to every value in $\overrightarrow{nec}$ to form a new scaled vector $\overrightarrow{nec_{cs}}$ for all the values of $\overrightarrow{nec_{cs}}$ that are below the noise floor are set to the noise floor.

The final step of forming the comparison vectors is to add to $\overrightarrow{cs}$ any peak values from the cross-spectra outside the Bragg at range-Doppler bins not contained in s, giving the new vector $\overrightarrow{cs}_{comp}$. A value equal to the noise floor is appended to $\overrightarrow{nec_{cs}}$ vector forming a new vector $\overrightarrow{nec}_{comp}$. The correlation, r_2, and L2 norm distance d between $\overrightarrow{cs}_{comp}$ and $\overrightarrow{nec}_{comp}$. The combination of nacelle angle and rotation rate, which simultaneous yields the smallest value of d and largest values of r_1 and r_2, is chosen as our most likely state of the system.

Department of the Interior (DOI)

The Department of the Interior protects and manages the Nation's natural resources and cultural heritage; provides scientific and other information about those resources; and honors the Nation's trust responsibilities or special commitments to American Indians, Alaska Natives, and affiliated island communities.

Bureau of Ocean Energy Management (BOEM)

The mission of the Bureau of Ocean Energy Management is to manage development of U.S. Outer Continental Shelf energy and mineral resources in an environmentally and economically responsible way.

BOEM Environmental Studies Program

The mission of the Environmental Studies Program is to provide the information needed to predict, assess, and manage impacts from offshore energy and marine mineral exploration, development, and production activities on human, marine, and coastal environments. The proposal, selection, research, review, collaboration, production, and dissemination of each of BOEM's Environmental Studies follows the DOI Code of Scientific and Scholarly Conduct, in support of a culture of scientific and professional integrity, as set out in the DOI Departmental Manual (305 DM 3).